SCIENCE CHINA
Physics, Mechanics & Astronomy

• Article •

October 2023 Vol. 66 No. 10: 104712
https://doi.org/10.1007/s11433-023-2168-0

An efficient multi-resolution SPH framework for multi-phase fluid-structure interactions

Chi Zhang[1,2], Yujie Zhu[3*], and Xiangyu Hu[1]

[1] *TUM School of Engineering and Design, Technical University of Munich, Garching 85748, Germany;*
[2] *Huawei Technologies Munich Research Center, Munich 80992, Germany;*
[3] *Xi'an Research Institute of Hi-Tech, Xi'an 710025, China*

Received April 3, 2023; accepted June 28, 2023; published online August 31, 2023

Applying different spatial and temporal resolutions for different sub-systems is an effective approach to increase computational efficiency for particle-based methods. However, it still has many challenges in terms of achieving an optimized computational efficiency and maintaining good numerical robustness and accuracy for the simulation of multi-phase flows involving large density ratio and interacting with rigid or flexible structures. In the present work, based on the multi-resolution smoothed particle hydrodynamics (SPH) method [Zhang et al., JCP 429, 110028 (2021)], an efficient multi-resolution SPH framework for multi-phase fluid-structure interactions (FSI) is proposed. First, an efficient multi-phase model, exploiting different density reinitialization strategies instead of applying different formulations to implement mass conservation to the light and heavy phases, respectively, is developed and the same artificial speed of sound for both phases can be used. Then, the transport velocity formulation is rewritten by applying temporal local flow state dependent background pressure to eliminate the unnatural voids, unrealistic phase separation and decrease the numerical dissipation. Finally, the one-sided Riemann-based solid boundary condition is modified to handle the FSI coupling in both single- and multi-resolution scenarios in the triple point. A set of examples involving multi-phase flows with high density ratio, complex interface and multi-phase FSI are studied to demonstrate the efficiency, accuracy and robustness of the present method.

multi-resolution method, smoothed particle hydrodynamics, multi-phase flows, multi-phase FSI

PACS number(s): 02.70.-c, 46.15.-x, 47.11.-j, 83.50.-v

Citation: C. Zhang, Y. Zhu, and X. Hu, An efficient multi-resolution SPH framework for multi-phase fluid-structure interactions, Sci. China-Phys. Mech. Astron. **66**, 104712 (2023), https://doi.org/10.1007/s11433-023-2168-0

1 Introduction

Multi-phase flow is ubiquitous in natural phenomena, e.g., rain drops, soap bubbles and water beading on a leaf. Extensive studies have been conducted in the past decades to unravel the underlying physics, address the associated large variety of engineering applications, e.g., thermal spray coating, ink-jet printing and multi-component flow in the chemical reactors. These problems always relate to the multi-phase flow involving large density ratio and interacting with rigid or flexible structures. Due to the intrinsic density discontinuity and complex physical interactions across the dynamically evolving material interface, numerical study of this type of problems is highly challenging [1, 2]. Conventional numerical flow solvers are Eulerian mesh-based methods, in which the evolution of moving interface calls for additional

*Corresponding author (email: yujiezhu1992@gmail.com)

interface tracking or capturing algorithms. Popular interface tracking algorithms include the volume of fluid method [3], the level-set method [4], the diffuse interface method [5], etc. However, they may suffer from serious numerical errors, instabilities and induce extra computational efforts, especially when flexible structures are displaced in multi-phase flow [6]. As an alternative, the fully Lagrangian and mesh-free methods, for instance, the smoothed particle hydrodynamics (SPH) which was originally developed by Lucy [7] and Gingold and Monaghan [8] for astrophysical applications, have shown peculiar advantages in handling multi-phase flows and fluid-structure interactions (FSI) [9-14]. Thanks to its fully Lagrangian nature, the SPH method shows instinctive advantage in handling complex material interface without additional interface tracking or capturing algorithms [15, 16].

Concerning the modeling of incompressible multi-phase flow and its interaction with rigid or flexible structure, the weakly-compressible (WC) assumption [17], where fluid pressure is calculated from density through an equation of state (EoS) with proper choice of artificial speed of sound, is widely applied in the literature [10, 11]. Notwithstanding its versatile applications and promising achievements, the WC-assumption induces spurious pressure oscillations and numerical instability problems, which exhibit unnatural voids and unrealistic phase separation in the simulation of multi-phase flow with high density ratio and violent interface change [10, 18, 19]. To remedy this issue, tremendous efforts have been conducted. Colagrossi and Landrini [10] proposed a multi-phase SPH method by adopting Moving Least Square (MLS) interpolation-based density reinitialization, using large surface tension for light phase and implementing XSPH correction [9] to realize isotropic particle distribution. This method can achieve stable modeling of multi-phase flows involving high density ratio and interacting with rigid structure, while greatly changes the natural physical property of the fluid [18] and introduces excessive computational costs by assigning the light phase 10 times larger artificial speed of sound than the one of the heavy phase [19]. Following ref. [10], efforts were devoted to avoiding unnatural void by applying particle shifting algorithm [20] and to producing smooth pressure field by introducing diffusive term in the continuity equation [21, 22]. However, the issue of excessive computational cost still hinders its further applications in large scale simulations. Hu and Adams [11] proposed a multi-phase SPH method for both macroscopic and mesoscopic flows by deriving the particle-averaged spatial derivative approximation from a particle smoothing function in which the neighboring particles only contribute to the specific volume, while maintaining mass conservation. This method can naturally handle density discontinuity across phase interface and achieve efficient simulation by assigning identical artificial speed of sound for both phases, while its applications to complex and violent interface are not fully addressed. Similar with ref. [11], Grenier et al. [23] proposed a Hamiltonian interface SPH formulation and introduced small repulsive force at the interface to capture sharp interface evolution. This method also suffers from low computational efficiency due to the large artificial speed of sound for light phase and requires extra sweeping and computational efforts for determining volume distribution of particle. Following the similar idea, Monaghan and Rafiee [24] developed a simple multi-phase SPH formulation by rewriting the repulsive force as the artificial stress formulation [25]. This method slightly improves the computational efficiency by reducing the artificial speed of sound of the light phase to 4 times larger than that of the heavy phase. Recently, Chen et al. [18] developed a multi-phase SPH method, which is different from the approach in ref. [10], by assuming the continuity of pressure and space across the interface and introducing corrected density reinitialization and positive background pressure to obtain smooth and positive pressure field. This method can achieve optimized computational efficiency as the same speed of sound is realized, while exhibits excessive numerical dissipation [18, 19]. Zheng and Chen [26] further proposed a modification with a first-order density reinitialization and a local implementation of the artificial viscosity. This modification demonstrates enhanced accuracy, such as shorter delays of the dynamics, due to less numerical dissipation induced. However, particles still undergo spurious fragmentation, particularly in the vicinity of phase interface in their violent water-air flow cases. More recently, Rezavand et al. [19] proposed a new multi-phase SPH method by exploiting the two-phase Riemann solver to handle the pairwise particle interaction and applying the transport-velocity formulation to the light phase. This multi-phase method assumes that the light phase experiences the heavy phase as moving boundary, while the heavy phase undergoes a free-surface-like flow. This method can achieve optimized computational efficiency by using the same artificial speed of sound for both phases, meanwhile effectively eliminates the unnatural voids and unrealistic phase separation.

In addition to applying the same artificial speed of sound for both phases, the computational efficiency can be further optimized by adopting multi-resolution scheme. Following this idea, the SPH method has experienced tremendous progresses in developing different accurate, stable and consistent multi-resolution schemes which can be generally classified into four families, i.e., adaptive particle refinement (APR) with or without particle splitting/merging [27-32], non-spherical particle scheme [33, 34], domain-decomposition based scheme [35-38] or the hybrid scheme

[39-41]. However, implementing multi-resolution scheme to particle-based incompressible multi-phase flow and FSI simulations has only been reported in recent years. Yang et al. [42, 43] proposed an adaptive spatial resolution (ASR) method [32] for multi-phase flows by varying the spatial resolution with respect to the distance to the interface and exploiting particle shifting technique with the consideration of variable smoothing length. Sun et al. [13] focused on the multi-phase hydroelastic FSI problems by adopting the multi-resolution scheme developed by Barcarolo et al. [39]. Zhang et al. [44] studied the multi-phase FSI problem by exploiting multi-resolution discretization strategy proposed by Zhang et al. [38] in fluid-structure interface while resolving the fluid interface by using the multi-phase model developed by Rezavand et al. [19] in single-resolution scenario. However, applying the multi-resolution framework [38] to multi-phase flows with large density ratio, in particular involving interaction with flexible structures, is still challenging and not addressed.

In this study, an efficient multi-resolution framework, where different spatial-temporal discretizations are applied for different sub-systems, is developed for multi-phase flows involving large density ratio and interacting with rigid or flexible structures. In cooperation with the multi-resolution framework presented by Zhang et al. [38], an efficient multi-phase model is proposed by introducing different density reinitialization strategies other than applying different formulations to implement mass conservation for the light and heavy phases, respectively, for the purpose of using the same artificial speed of sound for both phases. To decrease the numerical dissipation meanwhile preserve the feature of eliminating the unnatural voids and unrealistic phase separation, the transport-velocity formulation is rewritten by introducing a background pressure based on the temporal reference of current flow state. To handle fluid-structure coupling in single- and multi-resolution framework, the one-sided Riemann-based solid boundary condition [44, 45] is modified and adopted. A set of examples, e.g., multi-phase hydrostatic test, multi-phase flows with high density ratio and complex interface as well as multi-phase flows interacting with flexible structures, are studied to demonstrate the efficiency, accuracy and robustness of the present method. The numerical algorithms are implemented in the open-source SPHinXsys library [46, 47], and all the computational codes and data-sets accompanying this work are available at https://www.sphinxsys.org. This paper is organized as follows. Sect. 2 briefly summarizes the governing equations for both fluid and solid dynamics and sect. 3 presents the detailed methodology. Then, the numerical validations are presented and discussed in sect. 4, and concluding remarks are given in sect. 5.

2 Governing equations

In this paper, we consider the viscous and immiscible two-phase flow with large density ratio and its interaction with flexible structure which may experience large deformations. For the two-phase flow with large density ratio, i.e., $\rho_l/\rho_g \gg 1$ with ρ_l and ρ_g denoting the densities of light and heavy phase respectively, the mass and momentum conservation equations read

$$\begin{cases} \dfrac{\mathrm{d}\rho}{\mathrm{d}t} = -\rho\nabla\cdot\mathbf{v}, \\ \dfrac{\mathrm{d}\mathbf{v}}{\mathrm{d}t} = \dfrac{1}{\rho}\left[-\nabla p + \eta\nabla^2\mathbf{v}\right] + \mathbf{g} + \mathbf{f}^{s:p} + \mathbf{f}^{s:v}, \end{cases} \tag{1}$$

where $\frac{\mathrm{d}}{\mathrm{d}t} = \frac{\partial}{\partial t} + \mathbf{v}\cdot\nabla$ is the material derivative, ρ the density, $\mathbf{v}$ the velocity, p the pressure, η the dynamic viscosity, $\mathbf{g}$ the gravity. $\mathbf{f}^{s:p}$ and $\mathbf{f}^{s:v}$ represent the pressure and viscous force acting on the fluid due to the presence of rigid or flexible solid, respectively. With the weakly-compressible assumption [48] in mind, a linear EoS

$$p = c^{f\,2}(\rho - \rho^0), \tag{2}$$

for both the heavy and light phases is introduced to close the system of eq. (1). Here, ρ^0 is the initial reference density and $c^f = 10U_{\max}$ denotes the artificial speed of sound with $U_{\max}$ representing the maximum anticipated flow speed. Note that the compressible effect of the light phase is neglected following refs. [11, 12, 19, 23, 49]. Also, identical value for the artificial speed of sound is applied for both phases to optimize the computational efficiency as ref. [19].

For the flexible solid, an elastic and weakly-compressible material is considered. With the convention that the initial position $\mathbf{r}^0$ and the current position $\mathbf{r}$ of a material point are defined in the initial reference and the deformed current configuration, respectively, the deformation tensor $\mathbb{F}$ can be defined by

$$\mathbb{F} = \nabla^0\mathbf{u} + \mathbb{I}, \tag{3}$$

where $\nabla^0 \equiv \frac{\partial}{\partial \mathbf{r}^0}$ stands for the gradient operator with respect to the initial reference configuration, $\mathbf{u} = \mathbf{r} - \mathbf{r}^0$ the displacement and $\mathbb{I}$ the identity matrix. Here, the superscript $(\bullet)^0$ is introduced to denote the quantities in the initial reference configuration. Then, the mass and momentum conservation equations are defined following total Lagrangian framework as:

$$\begin{cases} \rho = \rho^0\frac{1}{J}, \\ \dfrac{\mathrm{d}\mathbf{v}}{\mathrm{d}t} = \dfrac{1}{\rho^0}\nabla^0\cdot\mathbb{P}^T + \mathbf{f}^{f:p} + \mathbf{f}^{f:v}, \end{cases} \tag{4}$$

where $J = \det(\mathbb{F})$ is the Jacobian determinant of deformation tensor $\mathbb{F}$, $\mathbb{P} = \mathbb{F}\mathbb{S}$ the first Piola-Kirchhoff stress tensor

with T denoting transpose operation and $\mathbb{S}$ the second Piola-Kirchhoff stress tensor. $\mathbf{f}^{f:p}$ and $\mathbf{f}^{f:\nu}$ represent the fluid pressure and viscous force acting on the solid, respectively. To close the system of eq. (4), the constitutive equation for linear elastic and isotropic material reads

$$\begin{aligned}\mathbb{S} &= K\,\mathrm{tr}\,(\mathbb{E})\,\mathbb{I} + 2G\left(\mathbb{E} - \frac{1}{3}\,\mathrm{tr}\,(\mathbb{E})\,\mathbb{I}\right)\\ &= \lambda\,\mathrm{tr}\,(\mathbb{E})\,\mathbb{I} + 2\mu\mathbb{E},\end{aligned} \tag{5}$$

where λ and μ are the Lam parameters [50], $K = \lambda + (2\mu/3)$ the bulk modulus and $G = \mu$ the shear modulus. As the weakly compressible material is considered, the corresponding artificial speed of sound is defined by $c^s = \sqrt{K/\rho}$. Note that, we introduce c^s to denote the sound speed of flexible structure to distinguish from the one c^f for fluid, viz., both light and heavy phases.

3 Methodology

In this section, we first present the extension of the multi-resolution framework [38] for multi-phase flow with light and heavy phases discrertized by different spatial resolutions using the Riemann-based SPH method. Then, the multi-phase density reinitialization strategy and the modified transport-velocity formulation are provided. Last but not least, the total Lagrangian formulations for discretizing solid dynamics and the fluid-solid interface treatment are detailed with time integration.

3.1 Multi-phase Riemann-based SPH

Following the multi-resolution framework where different smoothing lengths are applied to discretize different subsystems developed in ref. [38], we introduce h^l and h^h to denote the smoothing length for light and heavy phase discretizations, respectively. Similar with ref. [38], we assume that $h^l > h^h$, implying the dynamics of heavy phase is resolved at a higher spatial resolution, while the computational efficiency is enhanced when a lower resolution for the light phase is sufficient. Following refs. [19,45], the mass and momentum conservation equations of eq. (1) can be discretized with the Riemann-based SPH method as:

$$\begin{cases}\dfrac{\mathrm{d}\rho_i}{\mathrm{d}t} = 2\rho_i \sum_j V_j(\mathbf{v}_i - \mathbf{v}^*)\cdot\nabla_i W_{ij}^{h^\chi},\\ \dfrac{\mathrm{d}\mathbf{v}_i}{\mathrm{d}t} = -\dfrac{2}{m_i}\sum_j V_i V_j P^* \nabla_i W_{ij}^{h^\chi} + \dfrac{2}{m_i}\sum_j V_i V_j \dfrac{2\eta_i\eta_j}{\eta_i+\eta_j}\dfrac{\mathbf{v}_{ij}}{r_{ij}}\dfrac{\partial W_{ij}^{h^\chi}}{\partial r_{ij}}\\ \qquad\qquad +\mathbf{g} + \mathbf{f}_i^{s:p}(h^\chi) + \mathbf{f}_i^{s:\nu}(h^\chi),\end{cases} \tag{6}$$

where m is the particle mass, V particle volume, $\mathbf{v}_{ij} = \mathbf{v}_i - \mathbf{v}_j$ the relative velocity, $\mathbf{r}$ the particle position, $r_{ij} = |\mathbf{r}_i - \mathbf{r}_j|$ the particle distance and $\nabla_i W_{ij}^{h^\chi} = \frac{\mathbf{r}_i - \mathbf{r}_j}{r_{ij}}\frac{\partial W(r_{ij},h^\chi)}{\partial r_{ij}}$ is the gradient of the kernel function with respect to particle i. $\mathbf{v}^*$ and P^* are the solutions of an inter-particle Riemann problem along the unit vector $-\mathbf{e}_{ij} = \frac{\mathbf{r}_j - \mathbf{r}_i}{r_{ij}}$. Note that $h^\chi = h^l$ or $h^\chi = h^h$ is applied for particle interactions inside a single phase, i.e., light or heavy phase, while $h^\chi = h^l = \max(h^l, h^h)$ for particle interactions at the interface. In this case, $h^\chi = h^l$ is applied for both light and heavy phase particles located at the interface, indicating that the light phase particle i can be searched and tagged as a neighboring particle of a heavy phase particle j which is located in its neighborhood.

Following ref. [45], the initial left and right states of the inter-particle Riemann problem are reconstructed as:

$$\begin{cases}(\rho_L, U_L, p_L) = (\rho_i, -\mathbf{v}_i\cdot\mathbf{e}_{ij}, p_i),\\ (\rho_R, U_R, p_R) = (\rho_j, -\mathbf{v}_j\cdot\mathbf{e}_{ij}, p_j),\end{cases} \tag{7}$$

where subscripts L and R denote left and right states, respectively. With applying the dissipation limiter proposed by Zhang et al. [45] to the linearized Riemann solver, the Riemann solution can be obtained by

$$\begin{cases}U^* = \dfrac{\rho_L U_L + \rho_R U_R}{\rho_L + \rho_R} + \dfrac{p_L - p_R}{c(\rho_L + \rho_R)},\\ p^* = \dfrac{\rho_L p_R + \rho_R p_L}{\rho_L + \rho_R} + \dfrac{\rho_L\rho_R\beta(U_L - U_R)}{\rho_L + \rho_R}.\end{cases} \tag{8}$$

It is worth noting that the dissipation limiter $\beta = \min\left[3\max(U_L - U_R, 0), c^f\right]$ implying there is no numerical dissipation imposed when the fluid is under the action of an expansion wave and the numerical dissipation is modulated when the fluid is under the action of a compression wave [45]. With U^* in hand, $\mathbf{v}^*$ can be obtained by

$$\mathbf{v}^* = \left(U^* - \frac{\rho_L U_L + \rho_R U_R}{\rho_L + \rho_R}\right)\mathbf{e}_{ij} + \frac{\rho_i\mathbf{v}_i + \rho_j\mathbf{v}_j}{\rho_i + \rho_j}. \tag{9}$$

3.2 Density reinitialization for multi-phase flow

In ref. [19], a multi-phase model, where the light phase experiences the heavy phase like moving wall boundary while the heavy phase undergoes a free-surface-like flow, was proposed to eliminate non-physical voids or fragmentation meanwhile optimize the computational efficiency by applying the same value for the artificial speed of sound in both phases [10]. In particular, the density summation is applied in the light phase, while the continuity equation is dicretized for the heavy phase, to implement mass conservation. Different from this work, identical density evolution approach is applied for consistency in the present solver, while different density reinitialization strategies are introduced to the light and heavy phases. Specifically, the continuity equation is discretized by using eq. (6) for both phases, while the density field for heavy phase, which is treated as free surface

flow, is reinitialized at every advection time step [51] with the formulation following ref. [44]

$$\rho_i = \rho^0 \frac{\sum W\left(r_{ij}, h^h\right)}{\sum W^0\left(r_{ij}, h^h\right)} + \max\left[0,\ \rho^* - \rho^0 \frac{\sum W\left(r_{ij}, h^h\right)}{\sum W^0\left(r_{ij}, h^h\right)}\right] \frac{\rho^0}{\rho^*}. \tag{10}$$

For the light phase, internal flow is considered and eq. (10) can be simplified as:

$$\rho_i = \rho^0 \frac{\sum W(r_{ij}, h^\chi)}{\sum W^0\left(r_{ij}, h^\chi\right)}. \tag{11}$$

Here, ρ^* denotes the density before reinitialization. Note that the density reinitialization of the heavy phase ignores the presence of the light phase, whereas the light phase takes the heavy phase into account with $h^\chi = h^l$ for particle summation in the phase interface.

3.3 Transport-velocity formulation

Due to the tensile instability problem [25, 52], SPH method results particle clumping and unnatural void regions in the simulation of fluid dynamics when negative pressure presents [53]. For the simulation of multi-phase flow, in particular large density and complex interface involved, such issue becomes more severe and exhibits unnatural void region and phase separation [20]. To address this issue, particle shifting or transport-velocity formulations are developed in the literature [10, 13, 19, 44]. Here, the transport-velocity formulation [52-54] is adopted on particles of light phase, which is similar to the work in ref. [19] because the pressure of heavy phase is generally kept positive due to gravity. The particle advection velocity $\tilde{\mathbf{v}}$ is obtained by

$$\tilde{\mathbf{v}}_i(t+\delta t) = \mathbf{v}_i(t) + \delta t\left(\frac{\mathrm{d}\mathbf{v}_i}{\mathrm{d}t} - \frac{2}{m_i}\sum_j V_i V_j \widehat{p}_0 \nabla_i W_{ij}^{h^\chi}\right), \tag{12}$$

where $\widehat{p}_0$ denotes the background pressure [52, 53]. If a spatial-temporal constant background pressure of $\widehat{p}_0 = 4\rho^0 c^{f\,2}$ is applied [19], extra artificial damping would be induced due to the fact that transport-velocity formulation leads particle freezing. In this study, we modify the background pressure as $\widehat{p}_0 = 10\rho_i U_{\max}^2$ with $U_{\max}$ denoting the current maximum particle speed to decrease the artificial damping. Inspired by ref. [52] where a spatial-temporal localized background pressure is applied, the present modification is characterized by being spatial constant while temporal localized. The parameter of the background pressure is set according to numerical experiment and applied through all tests in this paper with the target of reducing artificial damping maximally meanwhile eliminating particle clumping effectively. Note that the light phase takes the heavy phase into account by applying the transport velocity with $h^\chi = h^l$ for particles at the interface.

3.4 Total Lagrangian formulation

Following refs. [38, 55], the discretization of the mass and momentum conservation equations of eq. (4) can be written in the total Lagrangian formulation as:

$$\begin{cases} \rho_a = \rho_a^0 \frac{1}{J}, \\ \dfrac{\mathrm{d}\mathbf{v}_a}{\mathrm{d}t} = \frac{1}{m_a}\sum_b V_a V_b \tilde{\mathbb{P}}_{ab} \nabla_a^0 W_{ab}^{h^s} + \mathbf{g} + \mathbf{f}_a^{f:p}\left(h^\chi\right) + \mathbf{f}_a^{f:\nu}\left(h^\chi\right), \end{cases} \tag{13}$$

where inter-particle averaged first Piola-Kirchhoff stress $\tilde{\mathbb{P}}$ reads

$$\tilde{\mathbb{P}}_{ab} = \frac{1}{2}\left(\mathbb{P}_a \mathbb{B}_a^0 + \mathbb{P}_b \mathbb{B}_b^0\right), \tag{14}$$

with adopting the correction matrix [38, 56, 57]

$$\mathbb{B}_a^0 = \left(\sum_b V_b^0\left(\mathbf{r}_b^0 - \mathbf{r}_a^0\right) \otimes \nabla_a^0 W_{ab}^{h^s}\right)^{-1} \tag{15}$$

to reproduce rigid-body rotation. Here, h^s is the smoothing length for discretizing the solid and $h^\chi = \max\left(h^s, h^k\right)$ with $k = l, h$ is determined by the corresponding fluid phase interacting with solid. Note that subscripts a and b are introduced to denote solid particles and the gradient of the kernel function

$$\nabla_a^0 W_{ab}^{h^s} = \frac{\partial W\left(\mathbf{r}_{ab}^0, h^s\right)}{\partial r_{ab}^0}\mathbf{e}_{ab}^0 \tag{16}$$

is evaluated at the initial reference configuration. Also, the first Piola-Kirchhoff stress tensor is computed from the constitutive law with the deformation tensor $\mathbb{F}$ given by

$$\mathbb{F}_a = \left(\sum_b V_b^0\left(\mathbf{u}_b - \mathbf{u}_a\right) \otimes \nabla_a^0 W_{ab}^{h^s}\right)\mathbb{B}_a^0 + \mathbb{I}. \tag{17}$$

Following ref. [58], the Kelvin-Voigt type artificial damping method is adopted to the total Lagrangian formulation to enhance the numerical stability for large strain dynamics.

3.5 Treatment of fluid-structure interface

In sect. 3.1, we have presented the implementation of the multi-resolution framework [38] to address the multi-resolution discretization for multi-phase flow. When implementing this framework to solve multi-phase FSI problems, one can apply three resolutions for different sub-systems, for example three-level discretization with $h^l = 2.0h^h = 4.0h^s$, as shown in the left panel of Figure 1. In this case, the computation efficiency can be maximally improved, while two

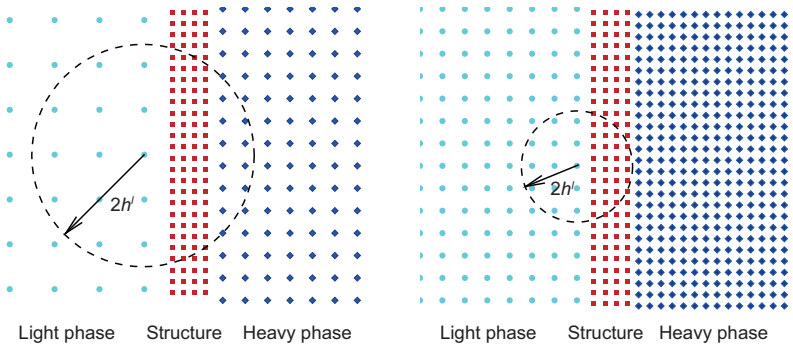

Figure 1 (Color online) Schematic illustration of the multi-phase FSI discretization in the present multi-resolution framework: Three-level discretization with $h^l = 2.0h^h = 4.0h^s$ (left panel) and two-level discretization $h^l = 2.0h^h = 2.0h^s$ (right panel).

drawbacks are also induced. First, the three-level discretization leads to a smoothing ratio of $h^l/h^s = 4$ between the light phase and structure which does not change the numerical accuracy of the FSI coupling while leads to less regular structure oscillations as demonstrated in ref. [38]. Second, the minimum particle resolution to discretize the structure should be properly chosen to avoid the nonphysical communications between fluid particles and another ones located on the other side of the structure, as shown in Figure 1 (left panel) where 4 layers of particles is applied to discretize the structure and the cut-off radius of $2.6dp$ is applied. Otherwise extra numerical treatment which is not the subjective of this paper should be implemented to avoid this nonphysical communications as ref. [59]. To avoid these drawbacks and achieve relatively high computational efficiency, the two-level discretization with $h^l = 2.0h^h = 2.0h^s$, as shown in Figure 1 (right panel), is adopted, in which multi-resolution discretization is applied to multi-phase and light-phase-structure coupling while single-resolution is for heavy-phase-structure coupling.

In the present method, the fluid-structure coupling is resolved by the generalized solid boundary condition proposed by Zhang et al. [44] where the flexible structure is behaving as a moving solid boundary for fluid and the solid boundary condition is imposed by exploiting a one-sided Riemann problem along the solid-normal direction as shown in Figure 2. Following refs. [44, 45], the pressure and viscous forces $\mathbf{f}_i^{s:p}$ and $\mathbf{f}_i^{s:\nu}$ in eq. (6) acting on a fluid particle i which can be light or heavy phase particle, due to the presence of the neighboring rigid or flexible solid particle a, are calculated from

$$\begin{cases} \mathbf{f}_i^{s:p}(h^\chi) = -\dfrac{2}{m_i}\sum_a V_i V_a p^* \nabla_i W_{ia}^{h^\chi}, \\ \mathbf{f}_i^{s:\nu}(h^\chi) = \dfrac{2}{m_i}\sum_a V_i V_a \dfrac{2\eta_i\eta_j}{\eta_i+\eta_j}\dfrac{\mathbf{v}_i - \mathbf{v}_a^d}{r_{ia}}\dfrac{\partial W_{ia}^{h^\chi}}{\partial r_{ia}}. \end{cases} \tag{18}$$

Here, $h^\chi = h^l$ and $h^\chi = h^h = h^s$ for light- and heavy-phase interacting with solid structure, respectively, with the assumption of $h^l = 2.0h^h = 2.0h^s$. In this case, both single- and multi-resolution couplings are simultaneously resolved in the triple point where light phase, heavy phase and structure particles meet as shown in Figure 2. For the one-sided Riemann problem, the left and right states are defined as [44, 45]:

$$\begin{cases} (\rho_L, U_L, p_L) = \left(\rho_f, -\mathbf{n}_a \cdot \mathbf{v}_i, p_i\right), \\ (\rho_R, U_R, p_R) = \left(\rho_a^d, -\mathbf{n}_a \cdot \mathbf{v}_a^d, p_a^d\right), \end{cases} \tag{19}$$

where $\mathbf{n}_a$ is the local normal vector pointing from solid to fluid, ρ_a^d and p_a^d are imaginary density and pressure, respectively. For non-slip boundary condition, the imaginary pressure p_a^d and velocity $\mathbf{v}_a^d$ in eq. (19) can be obtained by

$$\begin{cases} p_a^d = p_i + \rho_i \max\left(0, \left(\mathbf{g} - \dfrac{\widetilde{\mathrm{d}\mathbf{v}_a}}{\mathrm{d}t}\right)\cdot \mathbf{n}_a\right)(\mathbf{r}_{ia}\cdot\mathbf{n}_a), \\ \mathbf{v}_a^d = 2\mathbf{v}_i - \widetilde{\mathbf{v}}_a, \end{cases} \tag{20}$$

to address the force-calculation mismatch in multi-resolution scenario [38] by introducing the time averaged velocity $\widetilde{\mathbf{v}}_a$ and acceleration $\frac{\widetilde{\mathrm{d}\mathbf{v}_a}}{\mathrm{d}t}$ of solid particles over one fluid acoustic time step [51]. With the imaginary pressure p_a^d in hand, the imaginary density ρ_a^d can be calculated through the EoS presented in eq. (2). Accordingly, the fluid forces exerting on the solid structure, i.e., $\mathbf{f}_a^{f:p}$ and $\mathbf{f}_a^{f:\nu}$, can be obtained straightforwardly. Also, the one-sided Riemann solver is applied to the mass conservation equation in fluid-structure coupling. In the present FSI treatment, the influence of the solid to the fluid is resolved by a local particle-particle interaction pattern through the one-sided Riemann solver to compute the boundary flux by imposing proper boundary condition, i.e., non-slip solid boundary condition. Subsequently, it's straightforward to handle the FSI coupling in the triple point where single- and multi-resolution discretizations are co-exist.

Similar with ref. [44], particle penetration is observed for light phase in numerical experiments when light phase particles are entrapped during heavy phase impacting on the solid

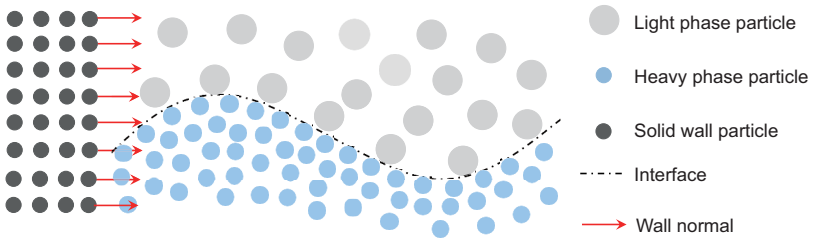

Figure 2 (Color online) Sketch of multi-phase particles interacting with solid particles along the normal direction through the one-side Riemann based scheme.

boundary. To address this issue, a penalty force between light-phase-structure interactions to repel the light-phase particles from the solid is adopted, which gives [44]

$$\mathbf{f}_i = -\frac{2}{m_i}\sum_j V_i V_a \Gamma(\mathbf{r}_i, \mathbf{r}_a)\,\mathbf{n}_a \frac{\partial W(\mathbf{r}_{ia}, h^\chi)}{\partial r_{ia}}. \tag{21}$$

The function $\Gamma(\mathbf{r}_i, \mathbf{r}_a)$ is defined by

$$\Gamma(\mathbf{r}_i, \mathbf{r}_a) = |p_i(\mathbf{r}_{ia}\cdot\mathbf{n}_a)| \begin{cases} (1.0-\beta)^2 \dfrac{0.01h^s}{h^\chi}, & \beta \le 1.0 \\ 0, & \beta > 1.0 \end{cases}. \tag{22}$$

Here, $h^\chi = h^l$ as the penalty force is only imposed on the light phase particles which are close to solid boundary. Parameter β is given by

$$\beta = 2.0\frac{\mathbf{r}_{ia}\cdot\mathbf{n}_a}{h^s}, \tag{23}$$

allowing a monotonically increasing penalty strength. Note that the imposing condition of parameter $\beta \le 1.0$ implies that there is no penalty force imposed for particle $2.0h^s$ faraway from the wall in its normal direction [44]. Also, there is no opposite force imposed on solid particles.

3.6 Time integration

To further optimize the computational efficiency, the dual-criteria time-stepping method [51] is adopted for time integration of fluids, where the advection criterion controls the updating of the particle-neighbor list as well as the corresponding computation of the kernel values and gradients, and the acoustic criterion determines the time integration of the physical variables. The advection criterion Δt_{ad} and the acoustic criterion Δt_{ac} are defined by

$$\begin{cases} \Delta t_{ad} = \min\left(\Delta t_{ad}^l, \Delta t_{ad}^h\right), \\ \Delta t_{ac} = \min\left(\Delta t_{ac}^l, \Delta t_{ac}^h\right), \end{cases} \tag{24}$$

where

$$\begin{cases} \Delta t_{ad}^i = 0.25\min\left(\dfrac{h^i}{U_{\max}}, \dfrac{h^{i^2}}{\eta}\right), \\ \Delta t_{ac}^i = 0.6\min\left(\dfrac{h^i}{c+U_{\max}}\right), \end{cases} \quad i = l, h. \tag{25}$$

Note that the single-time stepping method is applied for multi-phase coupling instead of the multi-time stepping scheme, which increases simulation complexity due to the requirement of surface particle detection of heavy phase and the corresponding operation of time average of physical states to enforce momentum conservation in the interface. In this case, moderate computational efficiency is achieved with the reward of not increasing the complexity of the present method.

At the beginning of each advection step, the fluid density field is reinitialized by eq. (10) or (11), the viscous force is computed and the transport-velocity formulation of eq. (12) is only applied for the light phase. During the advection criterion Δt_{ad}, the pressure relaxation process is conducted several acoustic time steps with the criterion Δt_{ac} by using the position-based Verlet scheme [38]. For each acoustic time step, the density and position of fluids are first updated to the mid-point as:

$$\begin{cases} \rho_i^{n+\frac{1}{2}} = \rho_i^n + \dfrac{1}{2}\Delta t_{ac}\dfrac{\mathrm{d}\rho_i}{\mathrm{d}t}, \\ \mathbf{r}_i^{n+\frac{1}{2}} = \mathbf{r}_i^n + \dfrac{1}{2}\Delta t_{ac}\mathbf{v}_i^n. \end{cases} \tag{26}$$

Then, the velocity of fluids is integrated to the new time step with

$$\mathbf{v}_i^{n+1} = \mathbf{v}_i^n + \Delta t_{ac}\frac{\mathrm{d}\mathbf{v}_i}{\mathrm{d}t}. \tag{27}$$

Finally, position and density of fluid are updated another half step as:

$$\begin{cases} \mathbf{r}_i^{n+1} = \mathbf{r}_i^{n+\frac{1}{2}} + \dfrac{1}{2}\Delta t_{ac}\mathbf{v}_i^{n+1}, \\ \rho_i^{n+1} = \rho_i^{n+\frac{1}{2}} + \dfrac{1}{2}\Delta t_{ac}\dfrac{\mathrm{d}\rho_i}{\mathrm{d}t}. \end{cases} \tag{28}$$

At this point, as one time step integration of fluids is completed, the pressure and viscous forces inducing acceleration to solid due to the existence of fluids are obtained by eq. (18)

and considered as constants during the time integration of solid with the criterion

$$\Delta t^s = 0.6 \min\left(\frac{h^s}{c^s + |\mathbf{v}|_{\max}}, \sqrt{\frac{h^s}{|\frac{\mathrm{d}\mathbf{v}}{\mathrm{d}t}|_{\max}}}\right), \tag{29}$$

where c^s is the artificial speed of sound of flexible solid. Following ref. [38], a multi-time stepping method is applied for the time integration of FSI coupling, implying $\kappa = [\frac{\Delta t_{ac}}{\Delta t^s}] + 1$ steps are conducted for solid during each acoustic time step size Δt_{ac} of fluids. We introduce herein index $\varkappa = 0, 1, ..., \kappa-1$ to denote integration step for solid. For each time step, the deformation tensor, density and position of solid are first updated to the midpoint as:

$$\begin{cases} \mathbb{F}_a^{\varkappa+\frac{1}{2}} = \mathbb{F}_a^{\varkappa} + \frac{1}{2}\Delta t^s \frac{\mathrm{d}\mathbb{F}_a}{\mathrm{d}t}, \\ \rho_a^{\varkappa+\frac{1}{2}} = \rho_a^0 \frac{1}{J}, \\ \mathbf{r}_a^{\varkappa+\frac{1}{2}} = \mathbf{r}_a^{\varkappa} + \frac{1}{2}\Delta t^s \mathbf{v}_a, \end{cases} \tag{30}$$

followed by the update of the velocity to a new time step with

$$\mathbf{v}_a^{\varkappa+1} = \mathbf{v}_a^{\varkappa} + \Delta t^s \frac{\mathrm{d}\mathbf{v}_a}{\mathrm{d}t}. \tag{31}$$

Finally, the deformation tensor, density and position of solid are updated to a new time step by

$$\begin{cases} \mathbb{F}_a^{\varkappa+1} = \mathbb{F}_a^{\varkappa+\frac{1}{2}} + \frac{1}{2}\Delta t^s \frac{\mathrm{d}\mathbb{F}_a}{\mathrm{d}t}, \\ \rho_a^{\varkappa+1} = \rho_a^0 \frac{1}{J}, \\ \mathbf{r}_a^{\varkappa+1} = \mathbf{r}_a^{\varkappa+\frac{1}{2}} + \frac{1}{2}\Delta t^s \mathbf{v}_a{}^{\varkappa+1}. \end{cases} \tag{32}$$

Note that the changing rate of deformation gradient $\frac{\mathrm{d}\mathbb{F}}{\mathrm{d}t}$ is computed through [55]

$$\frac{\mathrm{d}\mathbb{F}_a}{\mathrm{d}t} = \left(\sum_b V_b^0 (\mathbf{v}_b - \mathbf{v}_a) \otimes \nabla_a^0 W_{ab}\right) \mathbb{B}_a^0. \tag{33}$$

4 Numerical examples

In this section, several numerical examples of two-phase flow involving high-density ratio, complex phase change and interaction with rigid or flexible solid are investigated to assess the robustness, accuracy and efficiency of the present method by qualitative and quantitative comparison with experimental and numerical data in literature. In all tests, the 5th-order Wendland kernel [60] where smoothing length $h = 1.3\mathrm{d}p$ and support radius of $2h$ with $\mathrm{d}p$ denoting the initial particle spacing are applied. To setup the artificial speed of sound c^f, the maximum anticipated flow speed is estimated as $U_{\max} = 2\sqrt{gH}$, where H is the initial water depth, following the shallow-water theory [61] without special specification. Note that all cases are conducted based on the open-source SPHinXsys library in which the Intel TBB library, a shared-memory parallel library, is adopted.

4.1 Hydrostatic test

The first benchmark test we considered herein is a two-dimensional two-phase hydrostatic test in which gravity presents as shown in Figure 3 to assess the compatibility with the static solution and the ability of capturing sharp interface under high density ratio of the present method. Following ref. [19], the tank has a length of $L = 1$ and height of $H = 2L$ with the lower and upper half parts are filled with water and air, respectively. Both fluids are initially at rest and considered to be inviscid. We set water and air density as $\rho_w = 1$ and $\rho_a = 0.001$, respectively, resulting a density ratio of 1000. Note that unit gravity acceleration in negative y-direction is applied and all other quantities correspond to their non-dimensional variables. In the present simulation, particles are placed on a Cartesian lattice with particle spacing of $\mathrm{d}p^w = L/50$ for water discretization. For single- and multi-resolution simulations, we consider the water-air two cases with resolution ratio $\mathrm{d}p^a/\mathrm{d}p^w = 1$ and $\mathrm{d}p^a/\mathrm{d}p^w = 2$ to investigate the computational efficiency and accuracy.

Figure 4 portrays the particle distribution at $t = 50$ with density (left panel) and pressure (right panel) contours of the hydrostatic test in single- and multi-resolution scenarios. It can be evidently observed that a sharp interface without any notable nonphysical motion of water surface and a smooth pressure filed are obtained in both single- and multi-resolution simulations. The density and pressure contours of light phase in multi-resolution scenarios are presented in Figure 5. It is clear that the density and pressure profiles

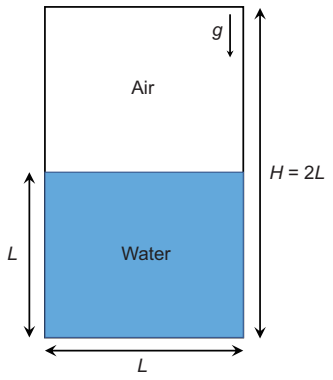

Figure 3 (Color online) Hydrostatic test: Schematic illustration.

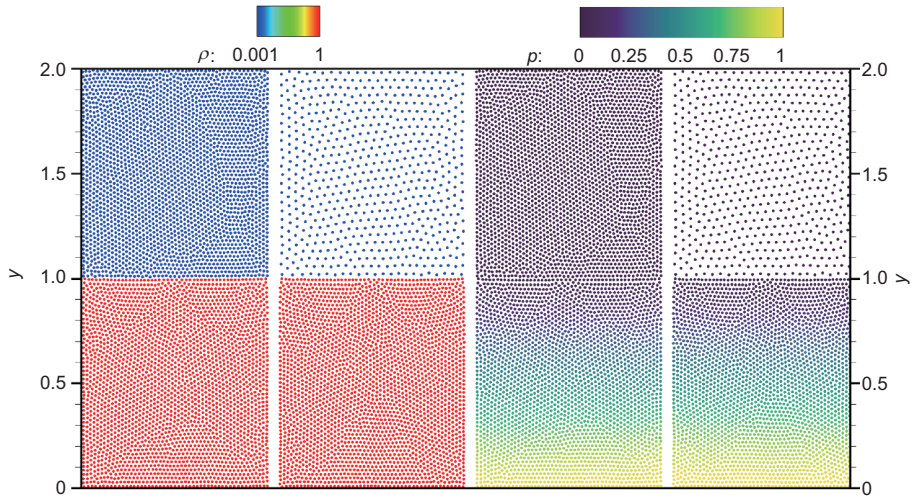

Figure 4 (Color online) Hydrostatic test: Particle distributions with density (left panel) and pressure contours (right panel) in single- and multi-resolution scenarios.

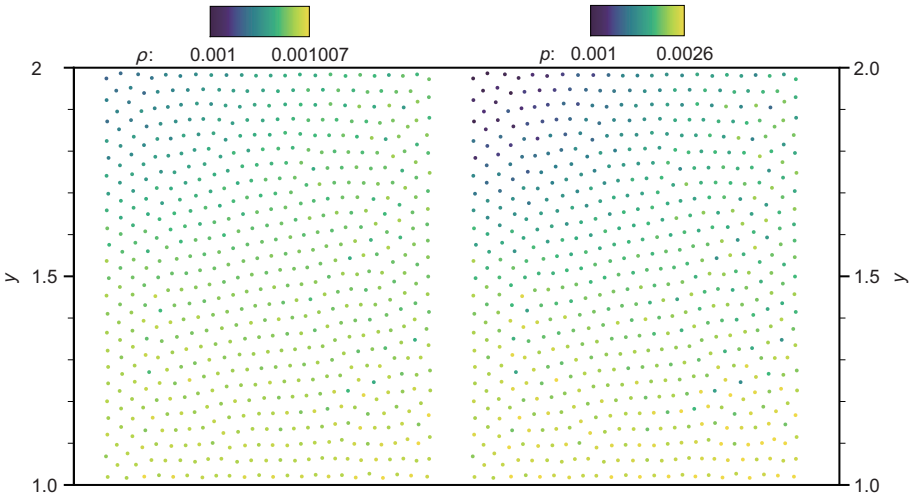

Figure 5 (Color online) Hydrostatic test: Density (left panel) and pressure contours (right panel) of light-phase in multi-resolution scenarios.

are reasonably reproduced except the slight noises induced by the weakly compressible assumption. These observations demonstrate the accuracy and robustness of the present method in capturing sharp interface and being compatible with hydrostatic solution without exhibiting nonphysical surface motion.

The accuracy of the present method is further quantitatively assessed by comparing the numerically computed pressure profile with the analytical hydrostatic pressure value. Figure 6 presents the time history of the numerical and analytical pressure signals probed at $y = 0.25H$. For both single- and multi-resolution computations, the obtained numerical pressure profile has a good agreement with the analytical values, demonstrating the accuracy of the present method. Furthermore, the energy conservation property is also investigated to show the substantial characteristic of the present method. Figure 7 plots the time evolution of the normalized mechanical energy defined as $\frac{E-E_0}{E_0}$ with E_0 denoting the initial value for single- and multi-resolution simulations. It can be observed that both the normalized mechanical energies decay to a very small value rapidly after an early-stage oscillations induced by the weakly-compressible model.

In general, the present method is compatible with hydrostatic solution and able to capture the sharp interface with high density ratio of 1000. Table 1 presents the comparison of CPU wall-clock time for multi- and single-resolution computation with the identical spatial resolution of heavy phase. It can be observed that the multi-resolution method achieves a speedup of 1.63 in comparison with single-resolution counterpart due to small number of particles used in light phase while almost identical numerical accuracy is obtained.

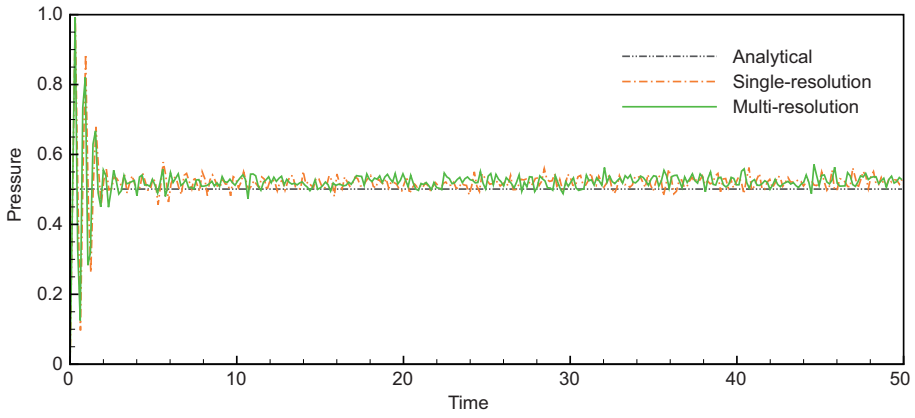

Figure 6 (Color online) Hydrostatic test: Time histories of the numerical and analytical pressures probed at $y = 0.25H$ in single- and multi-resolution scenarios.

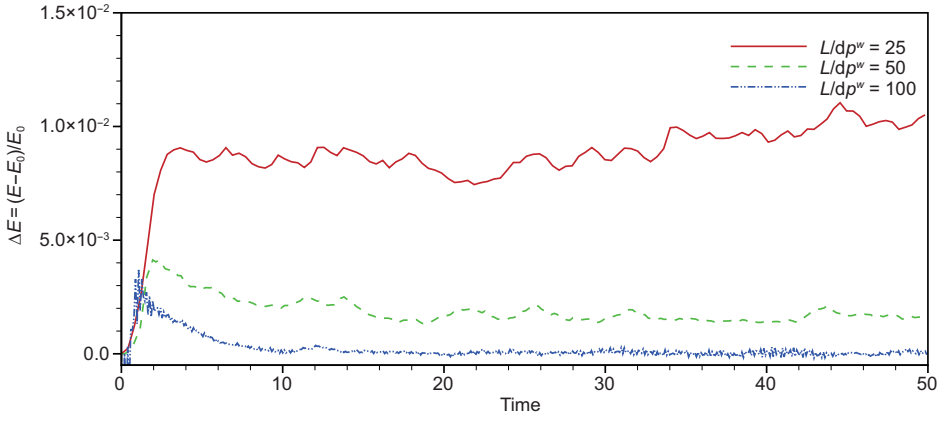

Figure 7 (Color online) Hydrostatic test: Time evolutions of the normalized mechanical energy in multi-resolution simulation.

Table 1 Hydrostatic test: Analysis of computational efficiency. The computations are carried out on an Intel(R) Xeon(R) L5520 2.27 GHz desktop computer with 24GiB RAM and a Scientific Linux operating system (6.9). To analyze the computational performance, we evaluate the CPU wall-clock time of $L/\mathrm{d}p^w = 100$ for shared memory parallelized computations (based on the Intel TBB library) until 50 time instant

Cases	Single resolution	Multi resolution	Speedup
Total particle numbers	20000	12500	–
CPU time (s)	741.7	453.71	1.63

4.2 Dam-break flow

In this section, we consider a two dimensional two-phase dam-break flow which exhibits complex interface change owing to violent wave impact and breaking events. As a benchmark test, this problem has been comprehensively studied in literature by experiments [62, 63] and numerical modeling [10, 19, 45, 64, 65] with or without considering the air phase. Following refs. [19, 45, 63], the schematic of this problem is illustrated in Figure 8. Initially, a water column with height of $H = 1$ and width of $2H$ is surrounded by air and located at the left corner of a tank with length $5.366H$ and height $2.5H$. In the present study, the flow is considered

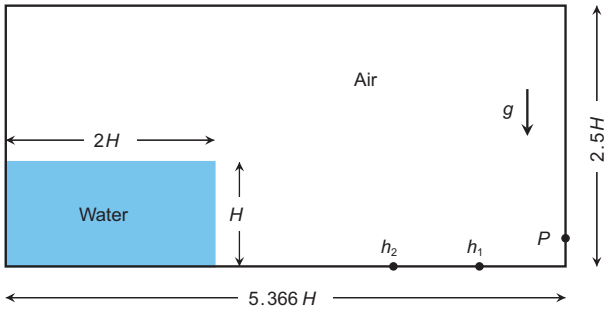

Figure 8 (Color online) Dam-break flow: Schematic illustration. Here, the pressure probe P is located at $y/H = 0.19$, and two surface sensors h_1 and h_2 are located at $x_2/H = 0.825$ and $x_2/H = 1.653$ away from the right wall, respectively.

to be inviscid and the density of water and air are set to $\rho_w = 1$ and $\rho_a = 0.001$, respectively, resulting a density ratio of 1000. With the gravity $g = -1$ in y-direction, all quantities correspond to their non-dimensional variables. Similar with refs. [19, 45], the water column with zero initial pressure is released immediately as the computation starts other than being released from an up-moving gate as in the experiment [62, 63], implying the pressure-relaxed water. For quantitative comparison, one pressure probe P located at the downstream wall at $y/H = 0.19$ [19, 65] and two surface sensors h_1 and h_2 respectively located at $x_2/H = 0.825$ and $x_2/H = 1.653$ away from the right wall are set for recording the impact pressure signal and water surface evolution. Following refs. [19, 65], the probe position is slightly shifted in comparison with the experimental setup [62] as suggested by Greco [66] to produce a better agreement. For multi-resolution simulations, we consider the water-air resolution ratio of $\mathrm{d}p^a/\mathrm{d}p^w = 2$.

Figure 9 illustrates several snapshots at different time instants for the water-air interface evolution obtained by the multi-resolution simulation. Similar with previous single-phase [45, 65, 67] and multi-phase [10, 19] simulation results, the main features of the dam-break flow, i.e., high roll-up along the downstream wall and the induced first jet due to its falling, the re-entry of the first jet and a large secondary reflective jet due to the backward wave motion, are well captured by the present multi-resolution simulation. More importantly, the sharp water-air interface is well maintained without exhibiting any unnatural void regions and unrealistic phase separation, implying the robustness of the present multi-resolution method.

To qualitatively assess the accuracy of the present method in capturing the complex interface evolution, the water-air interface profile at time instants of $t(\mathbf{g}/H)^{0.5} = 6.0$ and $t(\mathbf{g}/H)^{0.5} = 7.14$ is compared with those obtained by the boundary element method (BEM) [21], the level-set method [68] and the multi-phase SPH method [19]. In the present multi-resolution simulation with water-air resolution ratio of $\mathrm{d}p^a/\mathrm{d}p^w = 2$ and $H/\mathrm{d}p^w = 80$ which is identical to the one applied in ref. [19], a sharp water-air interface is well captured and maintained at time instant $t(\mathbf{g}/H)^{0.5} = 6.0$ before the re-entry of the backward wave as presented in Figure 10. The jet due to the falling of the run-up along the right-hand-side wall shows a good agreement with those predicted by the BEM [68] and SPH method [19]. Compared with the SPH prediction, the BEM result exhibits excessive numerical dissipation and shows considerable time delay of the backward wave, as can be observed in refs. [19, 21]. At the wave breaking stage at $t(\mathbf{g}/H)^{0.5} = 7.14$, a large secondary reflective jet and an entrapped air cavity are reasonably pre-

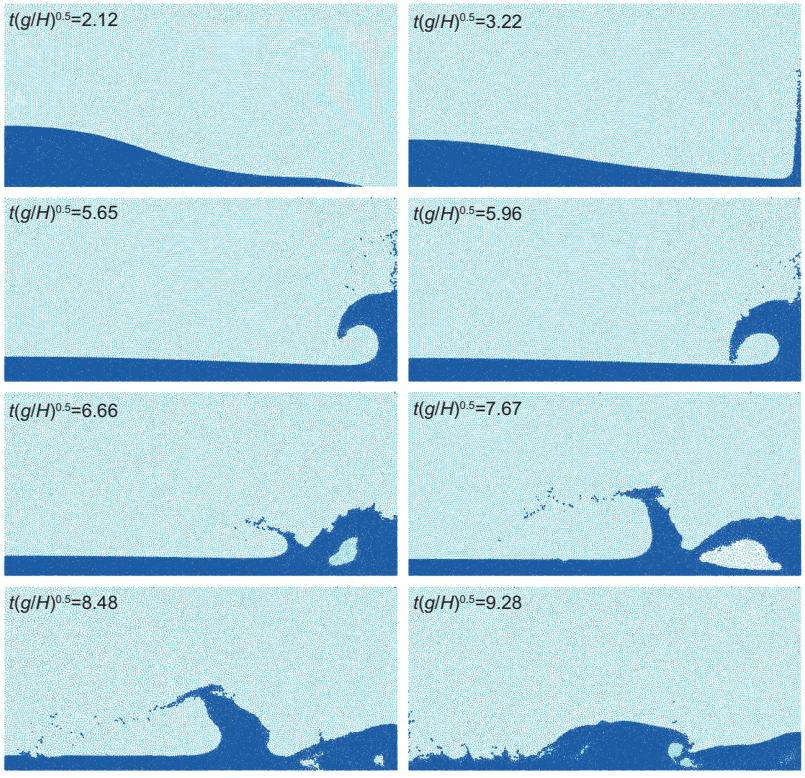

Figure 9 (Color online) Dam-break flow: Snapshots for the evolution of the water-air interface at different time instants obtained by the multi-resolution simulation.

dicted by the present multi-resolution method compared with those obtained by the level-set and multi-phase SPH methods [19,68], while slight discrepancies are noted due to the physical uncertainties induced by complex interface change. In general, the present multi-resolution method can accurately predict the complex interface, meanwhile, maintain a sharp phase interface without unnatural void region and exhibit less numerical dissipation and improved computational efficiency as discussed in the following part.

To demonstrate the low dissipation property of the modified transport-velocity formulation, we assess the numerical dissipation of the mechanical energy by defining [19,45,69]

$$\Delta E = \frac{E_k + E_p - E_p^0}{E_p^0 - E_p^\infty}, \tag{34}$$

where E_k is the kinetic energy, E_p the potential energy, E_p^0 the initial potential energy and E_p^∞ the potential energy when the flow reaches a hydrostatic state eventually. Figure 11 plots the time evolution of the numerical dissipation for mechanical energy in single- and multi-resolution simulations with different background pressures. In single-resolution simulation, the present modification of the background pressure evidently exhibits much less numerical dissipation. Besides, almost identical numerical dissipation is achieved by both single- and multi-resolution simulations with the present modification. In addition, a convergence study for the multi-resolution method with the background pressure modification is also depicted in Figure 11. It can be noted that the numerical dissipation is rapidly decreased with increasing spatial resolution.

Figure 12 plots the time history of the predicted water wave front in single- and multi-resolution simulations and its comparison with analytical solution obtained with shallow water theory [61], experimental data [63] and numerical results using multi-phase SPH method [19]. As expected, both single- and multi-resolution results have a good agreement with the theoretical shallow water solution, while show slight faster front wave propagation compared with the experimental observation due to the uncertainties of repeatability of experiment, wall roughness and the turbulence effects of boundary layer. Compared with the results presented in ref. [19], the present results show faster front wave propagation due to the modification of transport-velocity formulation and the implementation of solid boundary condition with Riemann-based scheme [44]. A convergence study of the present multi-resolution method is also reported in Figure 12. With the increase of spatial resolution, the numerical predicted propagation speed of the wave front is rapidly converged to the analytical solution with shallow water theory.

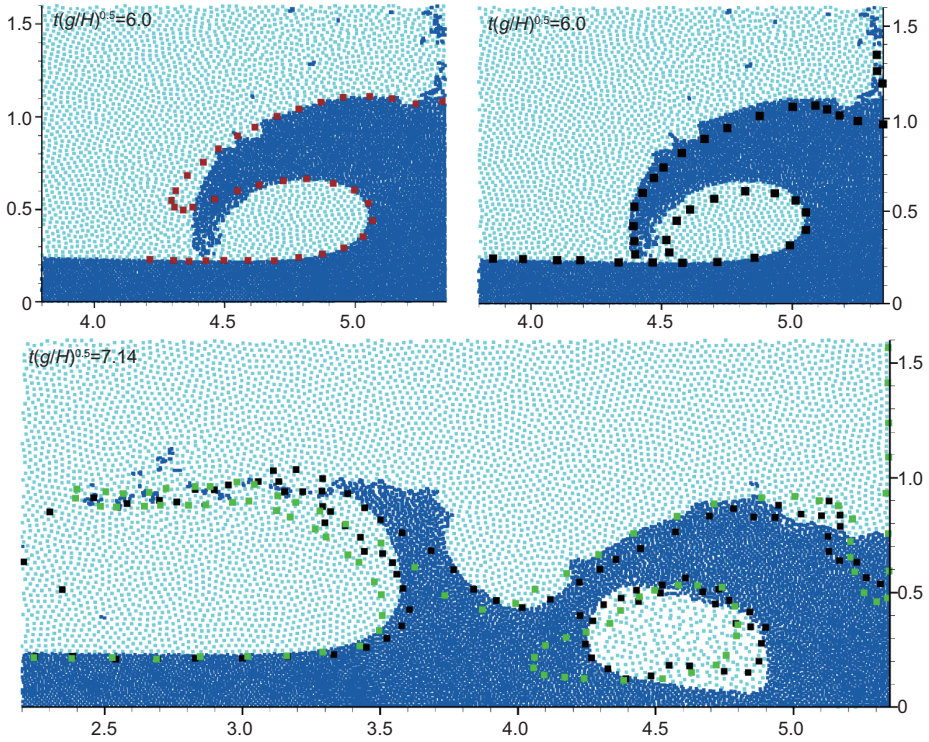

Figure 10 (Color online) Dam-break flow: Evolution of the water-air interface obtained by the present multi-resolution SPH method with $H/\mathrm{d}p^w = 80$, in comparison with those obtained by the BEM method (■) in ref. [21], the two-phase SPH method (■) in ref. [19] and the two-phase level-set method (■) in ref. [68].

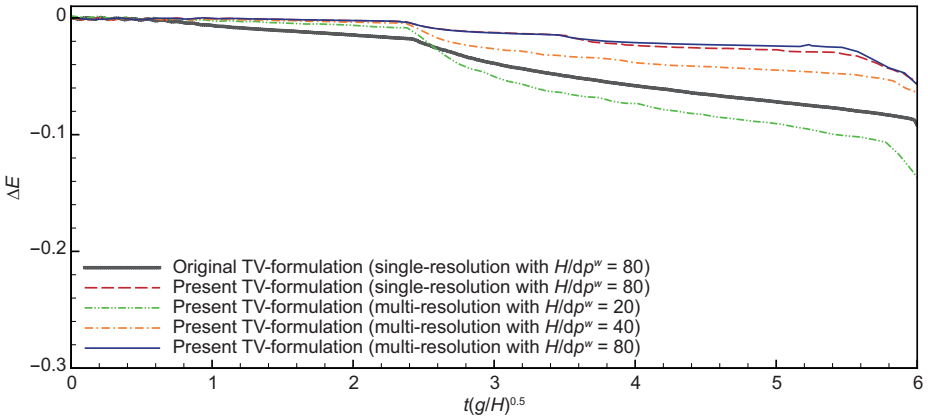

Figure 11 (Color online) Dam-break flow: The time history of the numerical dissipation of mechanical energy by using the present modified transport-velocity (TV) formulation with $\widehat{p}_0 = 10\rho_i U_{\max}^2$ with $U_{\max}$ the current maximum particle speed and the original one with $\widehat{p}_0 = 4\rho^0 c^{f\,2}$. Also, a convergence study is conducted for the present formulation.

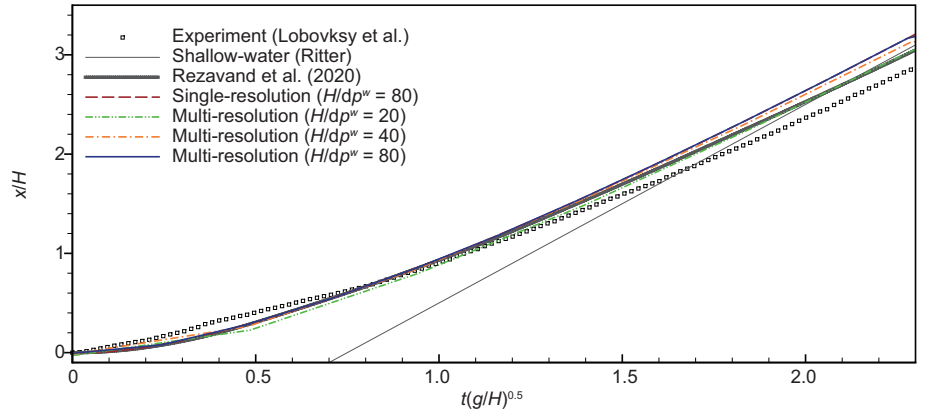

Figure 12 (Color online) Dam-break flow: The time history of the water wave front in single- and multi-resolution simulations in comparison with the analytical solution derived by shallow water theory [61], experimental data [63] and numerical results by using the multi-phase SPH method [19]. Note that a convergence study of the present multi-resolution method is also presented herein.

Note that the shallow water assumption does not hold at initial time instants of the dam-break flow.

Figure 13 depicts the time history of the water surface measured by sensors h_1 (upper panel) and h_2 (bottom panel) obtained by the present method in single- and multi-resolution scenarios, and its comparison with experimental and numerical data [19, 63]. As expected, the present results are in good agreement with the experimental observations [63] and previous numerical predictions [19]. Compared with the experimental data [63], a slightly faster wave front and a considerably higher backward wave are noted due to the inviscid model and the experimental uncertainty. Such discrepancies have also been observed in previous numerical studies in both single- and multi-phase simulations [19, 45]. In addition, a convergence study of the multi-resolution simulation is conducted herein. In particular, the time evolution of water surface on a longer time scale is evidently in good agreement with experiment with refined spatial resolutions. It is worth noting that the present prediction of water surface at h_1 shows a rapid convergence in capturing the correct temporal location, i.e., $t\,(\mathbf{g}/H)^{0.5} = 5.5$, of the backward wave, which is not achieved in the previous studies to the best knowledge of the authors.

Figure 14 plots the time history of the pressure signals probed by sensor P with the present method in single- and multi-resolution simulation and its comparison against experimental data [63] and numerical prediction obtained by the multi-phase SPH method [19]. As expected, the main pressure plateau agrees well with the experimental [63] and numerical data [63], while large oscillations, induced by the WC-assumption [19, 45, 65], are mitigated with increasing spatial resolution.

From the above qualitative and quantitative validations, the present multi-resolution method demonstrates its robustness and accuracy in capturing and maintaining sharp water-air interface without exhibiting unnatural voids and phase separation, predicting correct pressure signal during violent breaking and impact events, meanwhile achieves a computa-

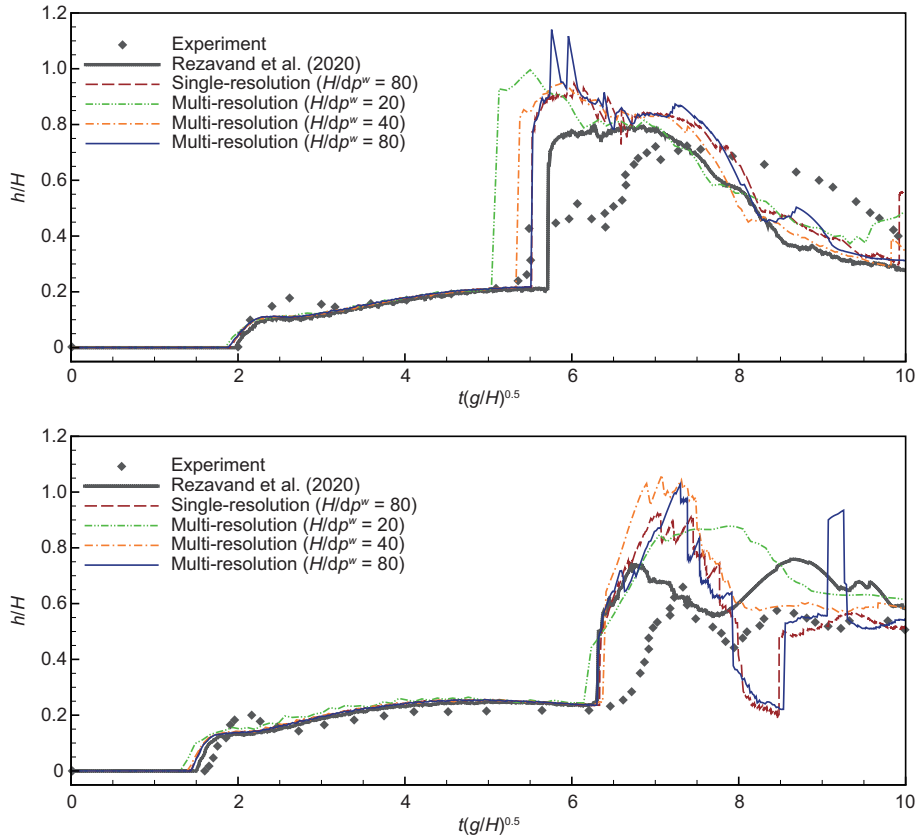

Figure 13 (Color online) Dam-break flow: The time evolution of the water surface probed at h_1 (upper panel) and h_2 (bottom panel) in single- and multi-resolution simulations and its comparison with experimental observation [63] and numerical result obtained by ref. [19]. The convergence study of the multi-resolution method is also presented herein.

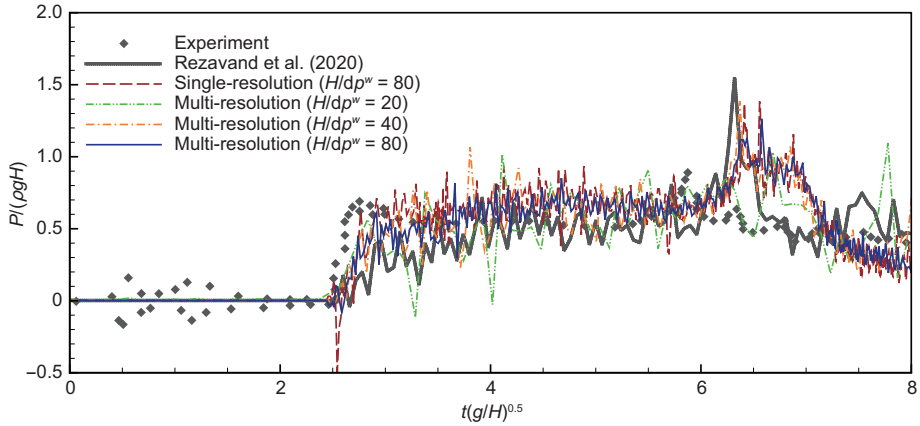

Figure 14 (Color online) Dam-break flow: The time history of the pressure signal probed by ensor P in single- and multi-resolution simulations and its comparison with experimental data [63] and numerical prediction [19]. Also, a convergence study of the present multi-resolution method is conducted herein.

tional speedup of 6.19 compared with single-resolution counterpart as shown in Table 2.

4.3 Nonlinear sloshing flow

The liquid sloshing phenomenon, which is characterized by violent and nonlinear surface motion induced by external excitation of the liquid container, occurs in various engineering applications. Typical examples include propellant sloshing in spacecraft tanks and rockets, and liquid cargo sloshing in ships and trucks transporting (e.g., oil and liquefied natural gas). Extensive numerical studies have been conducted in the literature [70] to understand the pressure fluctuation near the surface, acoustic effects due to the strong impact and im-

Table 2 Dam-break flow: Computational efficiency. To analyze the computational performance, we evaluate the CPU wall-clock time of the computation of $H/\mathrm{d}p^w = 80$ until 10 dimensionless time instant

Cases	Single resolution	Multi resolution	Speedup
Total particle numbers	85856	31064	–
CPU time (s)	2856.5	461.5	6.19

pacting loads on the container structure. These studies play a key role in preventing structure damage induced by sloshing flow, in particular when the tank motion frequency is close to the natural one of the inside liquid. Due to the advantage of capturing violent breaking and impact events [44, 45], SPH method has been widely applied in the study of sloshing phenomenon with or without considering air phase [71-74]. In this case, we consider a two-dimensional two-phase sloshing flow to investigate the air effects on impacting pressure and assess the robustness and accuracy of the present method.

Following the experimental study conducted by Rafiee et al. [71,74], a rectangular tank with a low filling water is taken into consideration. The tank with length of $L = 0.9$ m and height of $L = 0.9$ m is partially filled with water of height $h = 0.18$ m, while the remainder is filled by air, as in Figure 15. The flow is considered to be inviscid herein and the density of water and air are set to $\rho_w = 1000$ kg m^{-3} and $\rho_a = 1$ kg m^{-3}, respectively. The motion of the tank is driven by a sinusoidal excitation in x-direction with $x = A\sin(2.0f\pi t)$, where $A = 0.1$ m and $f = 0.496$ s^{-1} respectively denoting the amplitude and frequency. As f is close to the natural frequency of water, a resonant condition is created. For quantitative validation, three pressure sensors located on the left wall of the tank are applied to probe the impacting loads. To discretize the computational domain, the particles are placed on a regular lattice with particle spacing of $\mathrm{d}p = L/260$ and smoothing ratio of $h^a = 2h^w$.

Figure 16 portrays several snapshots of particle distributions with phase contour at different time instants in present multi-resolution simulation. Similar with the previous numerical results [19, 51, 75], the main features of a nonlinear sloshing flow, i.e., a traveling wave with a crest, the resulting bore impact and breaking as well as the high run-up along the tank walls, are well captured by the present method. With the presence of violent breaking, reentry and impact events of the water surface, the present multi-resolution simulation robustly captures and maintains a sharp water-air interface without exhibiting unnatural voids, nonphysical phase separation and particle penetration, implying the good performance of the proposed method in modeling complex and violent interface evolution.

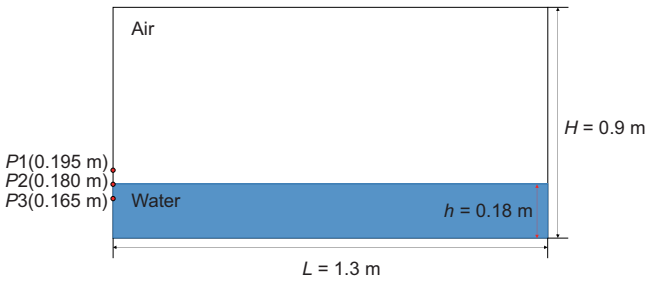

Figure 15 (Color online) Nonlinear sloshing flow: Schematic illustration. Note that there are three pressure sensors $P1$, $P2$ and $P3$ located on the left wall to probe the pressure signals.

To quantitatively assess the accuracy of the present method, Figure 17 depicts the time history of the numerical predicted impacting loads on the tank wall probed by sensors $P1$, $P2$ and $P3$ as well as their comparison against experimental data [71] and numerical result obtained by the single-phase SPH method [51]. It can be observed that both single- and multi-resolution results agree well with the experimental signal despite of some oscillations induced by WC-assumption. However, the impacting loads obtained by the simulations in single- and multi-resolution scenarios exhibit noticeable difference indicating the accuracy of the present multi-resolution solver. Compared with the results obtained with single-phase SPH method [51], the present multi-phase simulations show improved accuracy in capturing the main pressure plateau with smaller peak pressure. The underlying reason is that the air cushioning effect moderating the impact loads is properly captured and thus the accuracy of pressure field of water phase is further improved. Note that the compressibility of the air phase is neglected in the present simulation, as it complicates the evolution of the impacting loads which are strongly influenced by local phenomena, i.e., phase transition between liquid and vapor, liquid/gas mixture and surface tension, as noted by Dias and Ghidaglia [70].

In this test, the present multi-resolution method demonstrates its robustness and accuracy in modeling nonlinear liquid sloshing phenomenon. The optimized computational efficiency is achieved with a speedup of 23.76 compared with the single-resolution counterpart as shown in Table 3.

4.4 Dam-break flow impacting an elastic plate

In previous parts, the present method demonstrates its robustness and accuracy for modeling multi-phase flow with high-density ratio and violent interface evolution events such

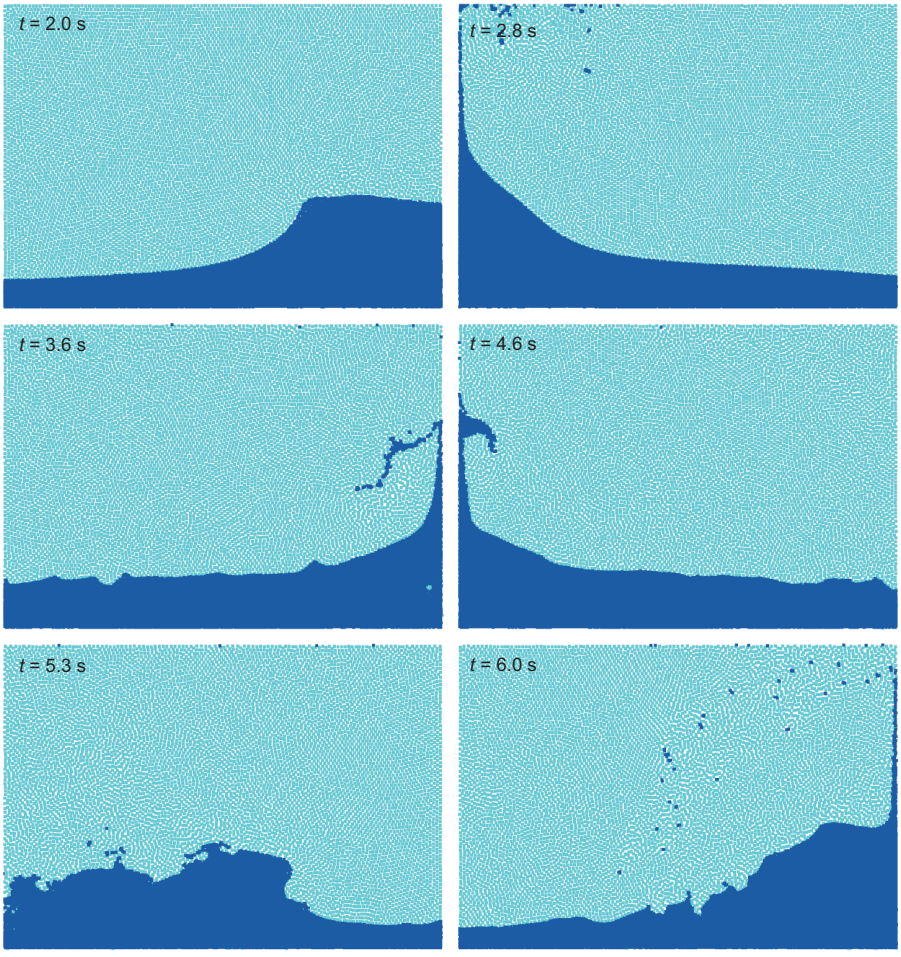

Figure 16 (Color online) Nonlinear sloshing flow: Snapshots of particle distributions at different time instants.

Table 3 Nonlinear sloshing flow: Analysis of computational efficiency. The computer information is reported in Table 1. For this test, we evaluate the CPU wall-clock time for computation until 10.0 s time instant

Cases	Single resolution	Multi resolution	Speedup
Total particle numbers	46800	18720	–
CPU time (s)	8708.5	366.5	23.76

as breaking and impact and hydroelstics multi-phased FSI problems. To further demonstrate its performance for violent multi-phase flow interacting with flexible structure, we consider herein a two-dimensional two-phase dam-break flow impacting on an elastic plate. This example has been studied as a benchmark test with both experimental and numerical data [13,44,76] available for qualitative and quantitative validations. Following the experimental setup in ref. [76], the dam-break flow is activated by a column of water with the size of height $H_w = 0.3$ m and length $L_w = 0.2$ m initially located at the left side of a tank with length $L_t = 0.8$ m and height $H_t = 0.6$ m whose reminder is filled with air, as portrayed in Figure 18. At the flow downstream, an elastic plate with the size of height $h = 0.09$ m and thickness $b = 0.004$ m is displaced 0.2 m far away from the right side wall of tank, as shown in Figure 18. Similar with refs. [13,44,76], the flow is considered to be inviscid and the density of water and air is respectively set as $\rho_w = 997$ kg m^{-3} and $\rho_a = 1.225$ kg m^{-3}, resulting a relatively high density ratio about 1000. As for the elastic plate, we consider a rubber-like material with density of $\rho_s = 1161.5$ kg m^{-3}, Young's modulus $E = 3.5$ MPa and Poisson ratio $\nu = 0.45$. To quantitatively validate the simulation accuracy, the horizontal displacement of the plate is measured by three markers on its middle line with different initial heights, i.e., Marker 1 at $h_1 = 0.0875$ m from the tank bottom, Marker 2 at $h_1 = 0.065$ m and Marker 3 at $h_1 =$

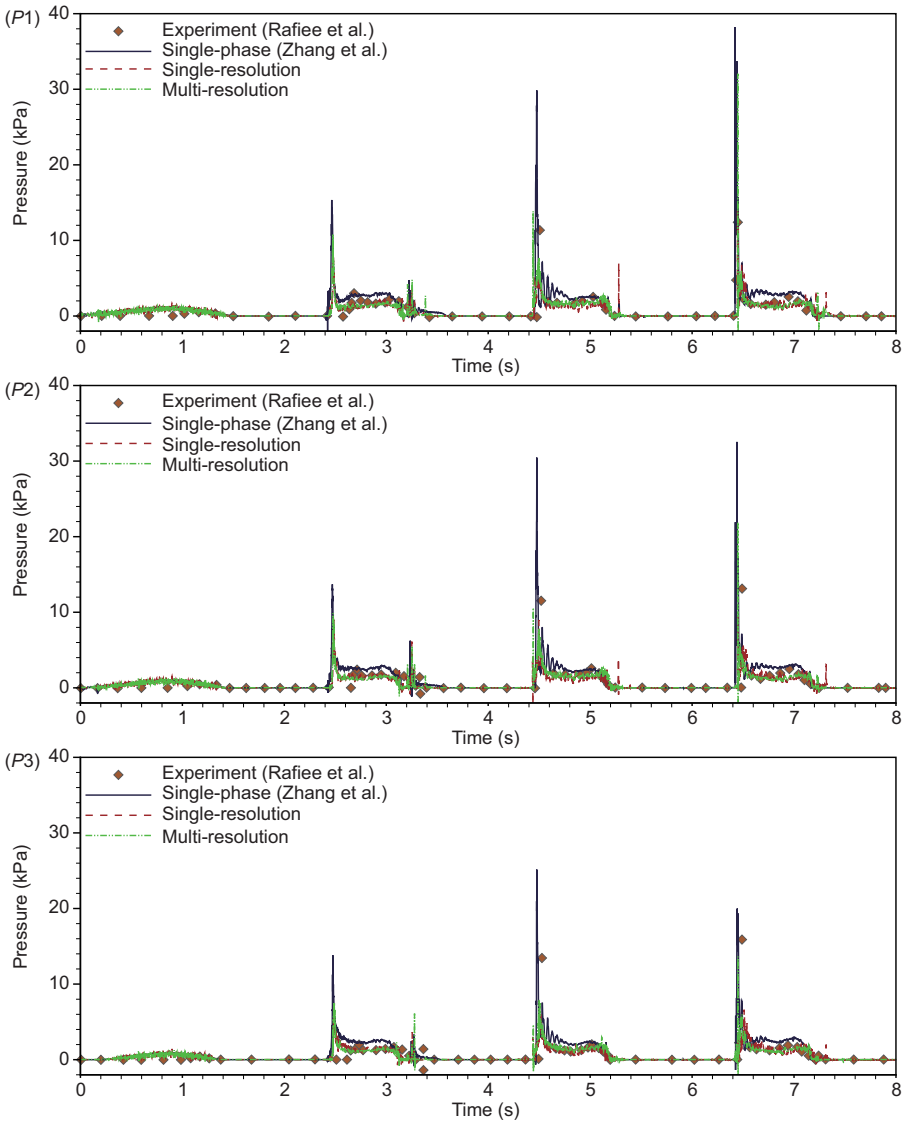

Figure 17 (Color online) Nonlinear sloshing flow: The time history of the impact pressure signals probed by sensors $P1$ $P2$ and $P3$, and its comparison against experimental data [71] and numerical results obtained by the single-phase SPH method [51].

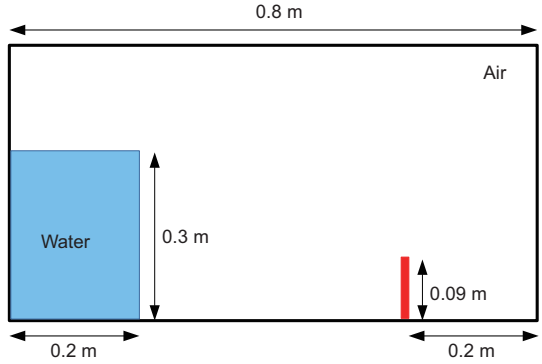

Figure 18 (Color online) Dam-break flow impacting an elastic plate: Schematic illustration. Note that the thickness of the flexible structure is $b = 0.004$ m and three markers with locations $h = 0.0875$ m (Marker 1) from the tan bottom, 0.065 m (Marker 2) and 0.04 m (Marker 3) are set for probing the horizontal displacement of the flexible plate.

0.04 m, as refs. [13, 44, 76]. In this paper, we consider two cases with different smoothing ratios, viz., Case-I of $\mathrm{d}p^a = 2.0\mathrm{d}p^w = 2.0\mathrm{d}p^s$ and Case-II of $\mathrm{d}p^a = \mathrm{d}p^w = \mathrm{d}p^s$, and both with the initial particle spacing of $\mathrm{d}p^s = b/4$.

Figure 19 depicts snapshots of the water-air interface evolution and the plate deflection at typical time instants for Case-I where the discretization is conducted in multi-resolution scenario. Before the water front impacting on the plate, a typical dam-break flow is observed with the flow propagating in the tank. At the impacting stage, the flow firstly bends the elastic plate, then overflows it and finally impacts on the right side wall of the tank, inducing two strong impact phenomena on both rigid and flexible structures. Similar with the previous numerical results [13, 44], the featured phenomena are well captured in the present multi-resolution

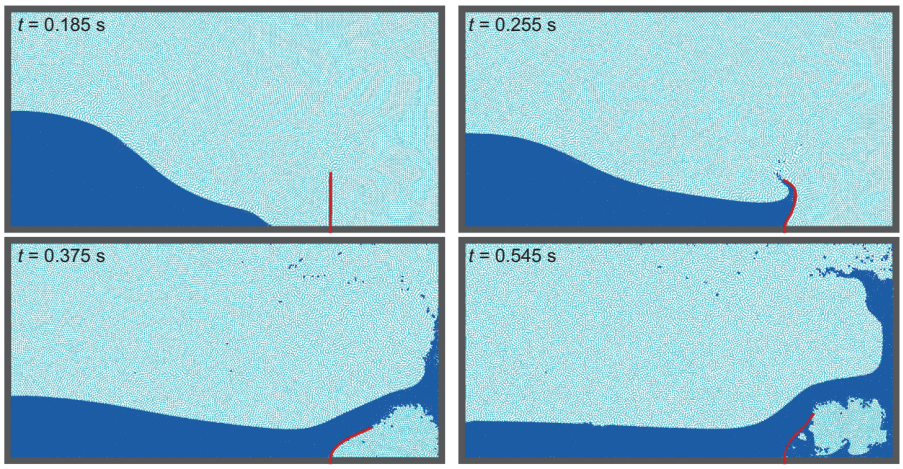

Figure 19 (Color online) Dam-break flow impacting an elastic plate: Snapshots of the water-air interface evolution and the plate deformation at different time instants for Case-I.

simulation. Also, the water-air interface is well captured and sharply maintained without exhibiting air particle penetration at both impact phenomena, demonstrating the robustness of present method. Note that as the results of Case-II do not exhibit visible difference from those reported in Figure 19 we refrain from showing them additionally.

Figure 20 portrays the particle distribution with pressure contour and the deformed configuration with von Mises stress contour of the plate at different time instants for Case-I, as well as the comparison against experimental observations presented by Liao et al. [76] and numerical results obtained by multi-phase δ-SPH method by Sun et al. [13]. In general, a qualitative good agreement on the interface evolution and the plate deflection is noted. Compared with the experimental observations [76], the water-air interface evolution and the plate deflection are reasonably predicted by the present multi-resolution method, which are similar as the FEM-DSM [76] and the multi-phase SPH methods [13, 44]. The main features observed in the experiment, i.e., a large splash jet induced by the water front impact and overflow, the disturbance of the cavity boundary induced by the plate vibration and the water droplets in the right corner after the secondary impact, are well captured. However, some discrepancies between the numerical results and the experimental observation are also noted. For example the numerical predicted overflow front composed by the splashing droplets is slightly smaller than the experimental observation due to the dominant three-dimensional effect and the overflow jet shows mistier water-air-interface after overflowing the plate due to the induced vibration, which will be shown in the following part of quantitative validation. These discrepancies are also observed in the numerical results obtained by different methods in literature [13, 44, 76]. Compared with the result obtained by multi-phase δ-SPH method of Sun et al. [13], the present one exhibits strong disturbance in the cavity boundary of the water overflow jet and noticeable separation between the jet and plate at time instants $t = 0.3$ s and $t = 0.35$ s, which is induced by model difference. In ref. [13], the multi-phase δ-SPH is applied with assigning the air an artificial speed of sound 10 times larger than the one of the water, adding background pressure in the EoS of both phases and implementing multi-phase tensile instability control algorithms. The present method [19] applies a more simple and efficient model, where same value is assigned to the artificial speed of sound for both phases and the background pressure is only applied to the transport-velocity formulation of the air.

To quantitatively validate accuracy, Figure 21 reports the time history of the horizontal displacement of the plate probed by Marker 1, 2 and 3 for Case-I and Case-II, as well as the comparison against experimental data [76], numerical prediction obtained with FDM-FEM method [76] and multi-phase δ-SPH method [13]. In general, the present method in both single- and multi-resolution scenarios demonstrates a good agreement with both the experimental and numerical data [13, 76] at the first impacting stage. At this stage, the displacement rapidly increases to its maximum value under the impulsive impacting force. As pointed out by Liao et al. [76], this stage is dominated by the first mode of vibration. However, discrepancy is observed afterward, for example, the displacement between time $t = 0.35$ s and $t = 0.85$ s at Marker 1 is underestimated by both the present and previous [13] multi-phase SPH methods compared with the experimental observation [76]. Compared with those reported by refs. [13, 76], the results obtained by FDM-FEM or multi-phase δ-SPH method, the present one can reasonably capture the higher modes of vibration (as shown in the zoom-in view of Figure 21) and the backward displacement of the

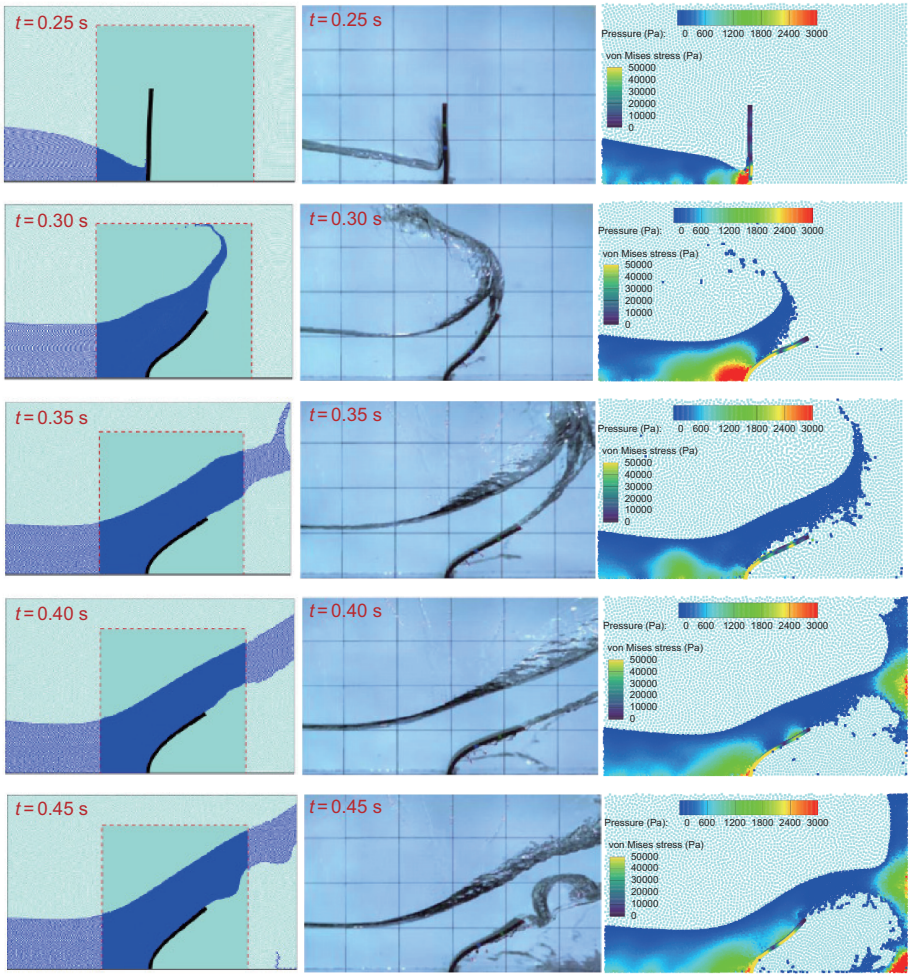

Figure 20 (Color online) Dam-break flow impacting an elastic plate: Snapshots at different time instants of particle distribution with pressure contour and the deformed configuration with von Mises stress contour of the plate at different time instants for Case-I. Here, the qualitative comparison is against experimental frames of Liao et al. [76] and numerical results obtained by multi-phase δ-SPH method of Sun et al. [13].

elastic plate observed at the final stage of the experiment, while slight difference is noted. It can be concluded that the present method and those in literature [13, 76] can well capture the first mode of vibration at the first impact stage, while the present one reasonably reproduces the higher modes of vibration and the backward deflection with slight discrepancies, which is likely associated with the stochastic nature of the impact pressures, the lack of exact repeatability of experiments and the effect of the roughness of boundary. It is worth noting that the present single- and multi-resolution simulations predict almost identical deflection of the plate except slight difference in the higher modes vibration, which exhibits large amplitude in the single resolution results implying the strong influence induced by air phase.

The above qualitative and quantitative validations demonstrate the robustness and accuracy of the present multi-resolution solver for capturing large structure deformation under strong impact. In addition, the present method achieves improved computational efficiency with speedup of 5.8 compared to single-resolution counterpart as shown in Table 4.

5 Concluding remarks

In this paper, an efficient and accurate multi-resolution SPH framework is proposed for multi-phase flow and hydroelastic FSI problems. To cooperate with the multi-resolution framework presented in ref. [38], a simple and efficient multi-phase SPH method is first proposed by introducing different density reinitialization strategies other than applying different evolution formulations to realize mass conservation. Then the transport velocity formulation is rewritten by applying localized background pressure to decrease the numerical dissipation. To capture the FSI coupling, the one-sided Riemann-based solid boundary condition is adopted

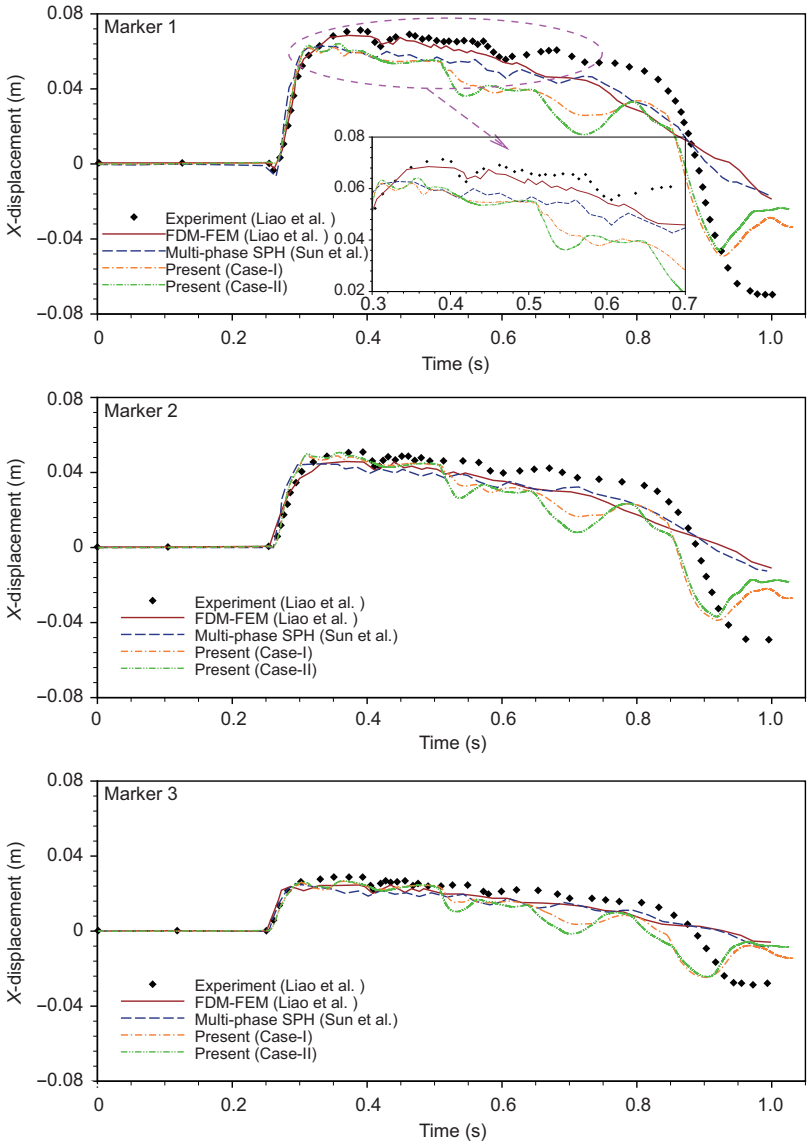

Figure 21 (Color online) Dam-break flow impacting an elastic plate: The time history of the horizontal displacement of the plate measured by Marker 1, 2 and 3 and its comparison with experimental data and FDM-FEM prediction from ref. [76] and multi-phase δ-SPH result of ref. [13].

Table 4 Dam-break flow impacting an elastic plate: Analysis of computational efficiency. The computer information is reported in Table 1. For this test, we evaluate the CPU wall-clock time for computation until 1.0 s time instant

Cases	Single resolution (Case-II)	Multi resolution (Case-I)	Speedup
Total particle numbers	480000	165270	–
CPU time (s)	2460.15	421.02	5.84

and modified in the multi-resolution scenario. In addition, the dual-criteria and multi-time steeping methods are applied for time integration to further improve computational efficiency. With several benchmark tests with high density ratio and complex phase interface, e.g., hydrostatic test, sloshing flow, dam-break flow and its interaction with rigid or flexible structures, the present method demonstrates its efficiency, accuracy and robustness. The performance of the present multi-resolution framework renders it a potential and practicable alternative in terms of computational efficiency for multi-physics applications in studying natural phenomena and engineering problems. In addition, when thin structure is involved, the present multi-resolution framework can be extended to "fluid-shell" interactions straightforwardly by

modifying the treatment of fluid-structure interface to further improve the computational efficiency with a suitable shell model, which is the subject of our future work.

This work was supported by the Deutsche Forschungsgemeinschaft (DFG) for their sponsorship of this research (Grant No. DFG HU1527/12-4). Yujie Zhu acknowledges the Natural Science Foundation of Shaanxi Province (Grant No. 2023-JC-QN-0052), and the National Natural Science Foundation of China (Grant No. 92152201).

1 T. Long, Z. Zhang, and M. Liu, Sci. China-Phys. Mech. Astron. **64**, 284711 (2021).
2 M. Liu, and Z. Zhang, Sci. China-Phys. Mech. Astron. **62**, 984701 (2019).
3 C. W. Hirt, and B. D. Nichols, J. Comput. Phys. **39**, 201 (1981).
4 M. Sussman, P. Smereka, and S. Osher, J. Comput. Phys. **114**, 146 (1994).
5 D. M. Anderson, G. B. McFadden, and A. A. Wheeler, Annu. Rev. Fluid Mech. **30**, 139 (1998).
6 E. Oñate, S. Idelsohn, O. Zienkiewicz, and R. Taylor, Int. J. Numer. Methods Eng. **39**, 3839 (1996).
7 L. B. Lucy, Astron. J. **82**, 1013 (1977).
8 R. A. Gingold, and J. J. Monaghan, Mon. Not. R. Astron. Soc. **181**, 375 (1977).
9 J. J. Monaghan, and A. Kocharyan, Comput. Phys. Commun. **87**, 225 (1995).
10 A. Colagrossi, and M. Landrini, J. Comput. Phys. **191**, 448 (2003).
11 X. Y. Hu, and N. A. Adams, J. Comput. Phys. **213**, 844 (2006).
12 A. Zhang, P. Sun, and F. Ming, Comput. Methods Appl. Mech. Eng. **294**, 189 (2015).
13 P. N. Sun, D. Le Touzé, and A. M. Zhang, Eng. Anal. Bound. Elem. **104**, 240 (2019).
14 Y. Zhu, C. Zhang, Y. Yu, and X. Hu, J. Hydrodyn. **33**, 195 (2021).
15 G. Tryggvason, B. Bunner, A. Esmaeeli, D. Juric, N. Al-Rawahi, W. Tauber, J. Han, S. Nas, and Y. J. Jan, J. Comput. Phys. **169**, 708 (2001).
16 S. Pan, X. Lyu, X. Y. Hu, and N. A. Adams, J. Comput. Phys. **354**, 311 (2018).
17 J. J. Monaghan, Annu. Rev. Astron. Astrophys. **30**, 543 (1992).
18 Z. Chen, Z. Zong, M. B. Liu, L. Zou, H. T. Li, and C. Shu, J. Comput. Phys. **283**, 169 (2015).
19 M. Rezavand, C. Zhang, and X. Hu, J. Comput. Phys. **402**, 109092 (2020).
20 A. Mokos, B. D. Rogers, and P. K. Stansby, J. Hydraulic Res. **55**, 143 (2017).
21 M. Antuono, A. Colagrossi, and S. Marrone, Comput. Phys. Commun. **183**, 2570 (2012).
22 I. Hammani, S. Marrone, A. Colagrossi, G. Oger, and D. Le Touzé, Comput. Methods Appl. Mech. Eng. **368**, 113189 (2020).
23 N. Grenier, M. Antuono, A. Colagrossi, D. Le Touzé, and B. Alessandrini, J. Comput. Phys. **228**, 8380 (2009).
24 J. J. Monaghan, and A. Rafiee, Int. J. Numer. Meth. Fluids **71**, 537 (2013).
25 J. J. Monaghan, J. Comput. Phys. **159**, 290 (2000).
26 B. X. Zheng, and Z. Chen, J. Comput. Phys. **382**, 177 (2019).
27 V. Springel, Mon. Not. R. Astron. Soc. **364**, 1105 (2005).
28 M. Lastiwka, N. Quinlan, and M. Basa, Int. J. Numer. Meth. Fluids **47**, 1403 (2005).
29 R. Vacondio, B. D. Rogers, P. K. Stansby, and P. Mignosa, Comput. Methods Appl. Mech. Eng. **300**, 442 (2016).
30 S. Khorasanizade, and J. M. M. Sousa, Int. J. Numer. Meth. Engng **106**, 397 (2016).
31 W. Hu, G. Guo, X. Hu, D. Negrut, Z. Xu, and W. Pan, Comput. Methods Appl. Mech. Eng. **347**, 402 (2019).
32 X. Yang, S. C. Kong, M. Liu, and Q. Liu, J. Comput. Phys. **443**, 110539 (2021).
33 M. B. Liu, G. R. Liu, and K. Y. Lam, Shock Waves **15**, 21 (2006).
34 J. M. Owen, J. V. Villumsen, P. R. Shapiro, and H. Martel, Astrophys. J. Soppl. S **116**, 155 (1998).
35 X. Bian, Z. Li, and G. E. Karniadakis, J. Comput. Phys. **297**, 132 (2015).
36 K. Shibata, S. Koshizuka, T. Matsunaga, and I. Masaie, Comput. Methods Appl. Mech. Eng. **325**, 434 (2017).
37 A. Khayyer, N. Tsuruta, Y. Shimizu, and H. Gotoh, Appl. Ocean Res. **82**, 397 (2019).
38 C. Zhang, M. Rezavand, and X. Hu, J. Comput. Phys. **429**, 110028 (2021).
39 D. A. Barcarolo, D. Le Touzé, G. Oger, and F. de Vuyst, J. Comput. Phys. **273**, 640 (2014).
40 M. Tanaka, R. Cardoso, and H. Bahai, J. Comput. Phys. **359**, 106 (2018).
41 P. Omidvar, P. K. Stansby, and B. D. Rogers, Int. J. Numer. Meth. Fluids **68**, 686 (2012).
42 X. Yang, and S. C. Kong, Comput. Phys. Commun. **239**, 112 (2019).
43 X. Yang, S. C. Kong, and Q. Liu, Phys. Rev. E **104**, 055308 (2021).
44 C. Zhang, Y. Zhu, X. Lyu, and X. Hu, Eur. J. Mech.-B Fluids **94**, 276 (2022).
45 C. Zhang, X. Y. Hu, and N. A. Adams, J. Comput. Phys. **335**, 605 (2017).
46 C. Zhang, M. Rezavand, Y. Zhu, Y. Yu, D. Wu, W. Zhang, S. Zhang, J. Wang, and X. Hu, Softw. Impacts **6**, 100033 (2020).
47 C. Zhang, M. Rezavand, Y. Zhu, Y. Yu, D. Wu, W. Zhang, J. Wang, and X. Hu, Comput. Phys. Commun. **267**, 108066 (2021).
48 J. P. Morris, P. J. Fox, and Y. Zhu, J. Comput. Phys. **136**, 214 (1997).
49 E. G. Flekkøy, P. V. Coveney, and G. De Fabritiis, Phys. Rev. E **62**, 2140 (2000).
50 I. S. Sokolnikoff, et al. collaboration of R. D. Specht, *Mathematical Theory of Elasticity*, Vol. 83 (McGraw-Hill, New York, 1956).
51 C. Zhang, M. Rezavand, and X. Hu, J. Comput. Phys. **404**, 109135 (2020).
52 C. Zhang, X. Y. Hu, and N. A. Adams, J. Comput. Phys. **337**, 216 (2017).
53 S. Adami, X. Y. Hu, and N. A. Adams, J. Comput. Phys. **241**, 292 (2013).
54 Y. Zhu, C. Zhang, and X. Hu, Comput. Fluids **230**, 105140 (2021).
55 C. Zhang, J. Wang, M. Rezavand, D. Wu, and X. Hu, Comput. Methods Appl. Mech. Eng. **381**, 113847 (2021).
56 R. Vignjevic, J. R. Reveles, and J. Campbell, *SPH in a Total Lagrangian Formalism* (CMC-Tech Science Press, New York, 2006), p. 181.
57 P. W. Randles, and L. D. Libersky, Comput. Methods Appl. Mech. Eng. **139**, 375 (1996).
58 C. Zhang, Y. Zhu, Y. Yu, D. Wu, M. Rezavand, S. Shao, and X. Hu, Eng. Anal. Bound. Elem. **143**, 1 (2022).
59 M. McLoone, and N. J. Quinlan, Eur. J. Mech.-B Fluids **92**, 117 (2022).

60 H. Wendland, Adv. Comput. Math. **4**, 389 (1995).
61 A. Ritter, Zeitschrift. Verein. Deutsch. Ingen. **36**, 947 (1982).
62 B. Buchner, *Green Water on Ship-Type Offshore Structures*, Dissertation for Doctoral Degree (University of Technology Delft, Delft, 2002).
63 L. Lobovský, E. Botia-Vera, F. Castellana, J. Mas-Soler, and A. Souto-Iglesias, J. Fluids Struct. **48**, 407 (2014).
64 P. P. Wang, Z. F. Meng, A. M. Zhang, F. R. Ming, and P. N. Sun, Comput. Methods Appl. Mech. Eng. **357**, 112580 (2019).
65 S. Adami, X. Y. Hu, and N. A. Adams, J. Comput. Phys. **231**, 7057 (2012).
66 M. Greco, *A Two-Dimensional Study of Green-Water Loading*, Dissertation for Doctoral Degree (Norwegian University of Science and Technology, Trondheim, 2001).
67 A. Ferrari, M. Dumbser, E. F. Toro, and A. Armanini, Comput. Fluids **38**, 1203 (2009).
68 G. Colicchio, M. Landrini, and J. R. Chaplin, J. Fluids Eng. **127**, 1111 (2005).
69 S. Marrone, A. Colagrossi, D. Le Touzé, and G. Graziani, J. Comput. Phys. **229**, 3652 (2010).
70 F. Dias, and J. M. Ghidaglia, Annu. Rev. Fluid Mech. **50**, 243 (2018).
71 A. Rafiee, F. Pistani, and K. Thiagarajan, Comput. Mech. **47**, 65 (2011).
72 H. Gotoh, A. Khayyer, H. Ikari, T. Arikawa, and K. Shimosako, Appl. Ocean Res. **46**, 104 (2014).
73 J. R. Shao, H. Q. Li, G. R. Liu, and M. B. Liu, Comput. Struct. **100-101**, 18 (2012).
74 A. Rafiee, S. Cummins, M. Rudman, and K. Thiagarajan, Eur. J. Mech.-B Fluids **36**, 1 (2012).
75 C. Zhang, G. M. Xiang, B. Wang, X. Y. Hu, and N. A. Adams, J. Comput. Phys. **392**, 1 (2019).
76 K. Liao, C. Hu, and M. Sueyoshi, Appl. Ocean Res. **50**, 192 (2015).